Coastal Engineering 127 (2017) 170–187

Contents lists available at ScienceDirect

Coastal Engineering

journal homepage: www.elsevier.com/locate/coastaleng

Generation and propagation of ship-borne waves - Solutions from a Boussinesq-type model

C. Gabriel David [a,*], Volker Roeber [b], Nils Goseberg [a,c], Torsten Schlurmann [a]

[a] Ludwig-Franzius-Institute for Hydraulic, Estuarine and Coastal Engineering, Leibniz Universität Hannover, Hannover, Germany
[b] International Research Institute of Disaster Science, Tohoku University, Sendai, Japan
[c] Department of Civil Engineering, Faculty of Engineering, University of Ottawa, Canada

ARTICLE INFO

Keywords:
Boussinesq-type equations
Ship waves
Vessel wake
Kelvin wedge
Waterway and port engineering

ABSTRACT

Ship-borne waves are of significant interest for the design of port and waterway infrastructure and the maintenance of its surrounding environment. Computation of these nonlinear and dispersive waves has mainly been focusing on their near-field generation as a fluid-body interaction problem. This study presents an approach for the computation of ship waves generated by a moving pressure disturbance with phase-resolving and depth-averaged equations. To support a wide range of applicability, the paper deals with the evolution of the vessel wedge compared to an analytical solution for sub-to supercritical speeds and the assessment of wave patterns from a broad range of pressure term dimensions, including cross-references to findings in other studies. The conducted numerical experiments showcase the typical response of a Boussinesq-type model to a simplified moving pressure disturbance and identify the main factors and criteria for ship-wave propagation in the far-field of a vessel. Finally, a unique field dataset underlines the capability of an extended Boussinesq-type model to compute the propagation of vessel waves over an irregular bathymetry.

1. Introduction

The mathematical description of vessel waves have been of interest to scientist and engineers since the late 19th century. In his seminal paper, Lord Kelvin (William Thomson) was the first to study a moving disturbance in deep water such as an immersed ship hull (Lord Kelvin (William Thomson), 1887). The outer limit of the disturbance and the center axis of the disturbance with respect to the forward propagation form an angle, which is known as Kelvin wedge. Havelock (1908) presented the mathematical framework to describe this angle as a function of the dimensionless depth Froude number $F_h = c_S/c_{sw}$, which is the ratio of ship velocity c_S to wave celerity in shallow water $c_{sw} = \sqrt{gh}$, with g the gravitational acceleration and h the local water depth. The so-called Havelock-angle extends the Kelvin wegde from 19.28° at $F_h < 1$, which then rapidly approaches 90° as the ship Froude number approaches unity. It then decreases for the super-critical cases ($F_h > 1$). From a design perspective, early records of relationships between sailing speed and local wave heights were presented by Franzius and Straub (1936). An in-depth analysis of existing literature paired with extensive laboratory studies on the effects of ship-induced wakes near-shore was presented by Johnson (1957) twenty years later. A study on waves generated by three different ferry types at various sailing speeds in combination with measurements taken at a number of distances from the sailing line indicated that both parameters investigated had an influence on the maximum wave heights generated by the ship's motion (see Nece et al., 1985); however, there was no particular indication as to how the measured wave heights evolved in the closer vicinity of any given shoreline. Soomere and Rannat (2003) and Torsvik et al. (2009) reported a field study elucidating the need for more research in the field of ship-wake shoreline interaction as the authors found unnaturally long wave components and energetic high amplitudes originating from fast ferries in the Tallinn bay; the non-linear aspects of the wakes were discussed in greater depth by Soomere (2007). The slender-ship approximation (Chen and Sharma, 1995) was then used to modify a Boussinesq-type model to account for the motion of a ship in a river by Dam et al. (2006, 2008) who reported fair agreement between the numerical model and a in-situ measured ship wake system.

The wave system generated by a moving vessel in an open or confined body of water can be distinguished by its primary and a secondary wave portion. The primary wave system is composed of a front wave, a lateral

* Corresponding author.
E-mail addresses: david@lufi.uni-hannover.de (C.G. David), roeber@irides.tohoku.ac.jp (V. Roeber), goseberg@lufi.uni-hannover.de (N. Goseberg), schlurmann@lufi.uni-hannover.de (T. Schlurmann).

http://dx.doi.org/10.1016/j.coastaleng.2017.07.001
Received 22 July 2016; Received in revised form 14 June 2017; Accepted 8 July 2017

water depression and a transverse stern wave (Verhagen, 1998) whereas the secondary wave system predominantly forms in the wake path of the ship's propagation with interference peaks (Schiereck, 2001). Wave heights and periods of such strongly non-linear and complex ship wakes generally depend on the type of vessel, its sailing speed, shape and geometry of the hull, trajectory of propagation, and its relative distance and direction with regard to a confining boundary (Verhagen, 1998). A large amount of studies addressing waterways empirically investigated how wave heights and run-up/run-down flow velocities depend on parameters such as the vessel's draft, distance to an embankment, length and beam width, cross-section area amongst more parameters. Governing empirical equations to determine the relevant design parameters are summarized in recent design guidelines (PIANC, 1987).

To date, only few studies have attempted to model a ship's motion through an approximation of a partially submerged hull by a moving pressure source. Chen and Uliczka (1999) implemented a slender body type hull into a shallow water model. Nascimento et al. (2009) modified FUNWAVE by incorporating a moving pressure source and used a single pressure distribution to simulate the effect of a moving ship hull. Afterwards Li and Sclavounos (2002) model an elliptic pressure disturbance representing the ship's hull, Nascimento et al. (2011) extended the existing model - now called FUNWAVE + ship - to accommodate for multiple moving pressure sources and demonstrated general usefulness to the approach. It is however not clear whether the distribution or the speed of the pressure disturbance governs the generated wave-wake system in the far field. The first description of a pressure-term implementation with focus on the numerical implementation into a Boussinesq-type model was done by Bayraktar and Beji (2013).

Particularly the interaction of ship-induced wave-wake systems with sloped embankments, coastal and river shores as well as vertical structures such as quay walls has been of persistent interest to planers and engineers. Besides engineering design considerations that relate to the stability of revetments or loadings of vertical support structures, the motion of water as induced by waves and currents in the estuarine intertidal or littoral zone has a direct impact on the ecology. In recent years, the focus of hydraulic and coastal engineers shifted towards investigating environmentally friendly bank protection measures over purely technical solutions (e.g. Houser, 2010; De Roo and Troch, 2013, 2015). Maintenance-related analysis of revetment failure in estuarine waters often requires profound knowledge of the effects of ship wakes on specific locations along the embankment in order to properly design revetment restoration (Ohle and Zimmermann, 2001). Understanding the seasonality of beach sediment dynamics and at the same time assessing the bathing risks for swimmers equally requires ship-induced wave heights and periods as was reported by Velegrakis et al. (2007) in the context of high-energetic fast ferry wakes observed close to the port of Mytilene, Greece. An unusual tidal creek blockage bordering the Houston Ship Channel in 2005 was attributed to sediment transport cyclically transported by a ship-induced bore (Ravens and Thomas, 2008). Accurate information of ship wake heights along river shorelines may facilitate the analysis of emergent plant health subjected to motorboat wash as addressed by Bonham (1983); the relatively high influence of ship wash on submerged vegetation at 3 locations of the river Nile was stressed by Ali et al. (1999). The study also attributed differences in organic matter content to the influence of the ship wakes. In order to avoid excessive bank erosion, today's embankment management plans attempt to provide sheltered zones of no-wash in order to preserve or increase the abundance of macrobenthic infauna; in a recent study it was reasoned that established no-wash areas minimized the effect of boat wash (Bishop, 2004). An investigation on critical thresholds for an intertidal flat to shift from bare-earth to vegetated states found that the establishment of pioneer plants is limited to conditions where ship-induced long wave components are negligible (Silinski et al., 2015).

Data for ship-induced forces on vertical structures is also needed for harbor design and for the assessment of structural design live. All this underpins the necessity to enable planners and designers to simulate ship-related water motion. Although physical models (Silinski et al., 2015) or in-situ studies (De Roo and Troch, 2013) can be a viable option, oftentimes questions need to be answered for a greater variety of parameters and thus, there is an immediate need to have a simple yet accurate numerical model technique at hand to tackle some of the addressed applications.

Therefore, the present work utilizes a Boussinesq-type wave model (Roeber et al., 2010; Roeber and Cheung, 2012) with additional pressure terms to represent ship-induced free surface oscillations -henceforth called ship wakes-in the far field of a moving vessel in a parametric study; it is attempted to elucidate governing parameters and to present guidance on how to make use of such model in practical applications. The overall goal is to provide means to determine maximum wave heights related to sailing speeds covering the range of sub- and super-critical ship motion as well as to arbitrary hull forms. These will be useful for the design of sloped and vertical shoreline infrastructure for generalized cases extending validity of existing guidelines. The current work distinguishes from more specific work related to the ship-wave interaction in the ships' near fields predominantly accomplished by naval architects that concerns the feedback of the ship motion on the wave field and vice-versa (Miyata and Nishimura, 1985; Nakos and Sclavounos, 1994; Bal, 2008).

This study moreover aims at providing a unified numerical tool to simulate and assess ship wakes for their far field interaction with the shoreline as generated by any moving vessel under the assumption of linear trajectories along a water body boundary at arbitrary angles with respect to the shoreline.

Boussinesq-type wave models have received a lot of attention in the coastal engineering community. Their balance between accuracy and computation demand makes them suitable for applications such as long wave propagation, coastal engineering, harbor wave studies, sediment transport, and near-shore process investigations (Brocchini, 2013). Based on Boussinesq's seminal work describing propagation of water waves over horizontal bottom, many improvements were made to shape and render mathematical description of Boussinesq-type equations (BTE) more precise. Few outstanding contributions are highlighted here. Peregrine (1967) derived a set of BTE for varying bathymetry. Witting (1984) used a conservation form of the BTE and through higher-order expansions allowed for waves to be represented up to $kh_0 \geq 8$, with k the wave number and h_0 the water depth in deep water. A new form of the BTE was presented by Madsen et al. (1991) who improved the linear dispersion characteristics in intermediate water depth over horizontal bottom; their set of equations governed non-uniform bottom cases described in a follow-up paper (Madsen and Soerensen, 1992). An alternate approach with respect to linear dispersion was presented by Nwogu (1993) who suggested to evaluate the velocity variables close to the mid-depth of the water column. Lynett and Liu (2004) presented the first two-layer model with separate velocity profiles for the two layers to represent linear waves up to $kh_0 \approx 6$ for both first and second order. To extend the applicability of BTE to surfzone processes, equations have been developed, which include approximations of the vertical vorticity structure Briganti et al. (2004) to account for wave breaking. The equations, however, become rather lengthy over the 2D horizontal plane and thus more compact formulations have recently evolved. BTE based on conserved variables (momentum instead of particle speed) facilitate the use of Finite Volume schemes to integrate shock-capturing capabilities and dispersion-preserving characteristics. Such equations have shown to be useful to study breaking waves over complex bathymetries (e.g. Roeber et al., 2010; Roeber and Cheung, 2012; Roeber and Bricker, 2015). A set of fully non-linear BTE with improved vertical vorticity correction, and similar robust shock-capturing and wetting-drying algorithm was presented by Shi et al. (2012) as an improvement to the existing FUNWAVE code. Shock-capturing Finite Volume schemes have been used in numerous studies in combination with Nonlinear Shallow Water equations (NLSWE) and could potentially also be used with a new group of dispersive NSWE (e.g. Antuono et al., 2009). A comprehensive summary of Boussinesq-type models can be found in Brocchini (2013).

The current study thus seeks to address the following questions and objectives derived from the above given context:

- Present the extensions of a Boussinesq-type model - in this case the Boussinesq Ocean and Surf Zone (BOSZ) model by Roeber and Cheung (2012) - for the computation of a moving pressure disturbance of various shapes and for potentially arbitrary trajectories.
- Showcase a validation method for depth-averaged, phase-resolving wave models, based on an analytical approach for highly dispersive and non-linear waves.
- Investigate the general aspects of different pressure distribution shapes in the horizontal plane and the pressure magnitudes; also whether there is a relationship between the pressure magnitude and the draft of a prototype ship. This is achieved by using a systematic approach, determining the determining parameters for ship wake generation.
- Validate the extended model with a unique field data set involving ships of known hull shape and draft in an estuarine environment.

This study highlights that a Boussinesq-type numerical model can accurately compute far-field ship-induced waves through the definition of a simple pressure source term. As a second novel aspect, this work systematically investigates how the pressure term's distribution and the propagation speed affect characteristic wave parameters such amplitude, period, and Havelock's angle as well as the wake pattern. The implementation of the ship-wave generating pressure term is a useful extension for depth-integrated free-surface resolving wave models. As an example for such models, it is further demonstrated how the numerical model BOSZ (Roeber and Cheung, 2012), which previously had been validated with a series of benchmarking problems, is able to compute far-field ship-induced waves.

The paper is organized as follows: Section 2 outlines the mathematical background of the applied Boussinesq model, while Section 3 describes the utilization of the pressure terms to approximate a ship hull. Model validation (Section 5) and discussion of effects on the basic wave properties due to pressure term aspect ratios (Section 6) are presented for a basic computational domain in Section 4. A real-world data set is used subsequently to validate the numerical code applying it to a section of the river Elbe close to Hamburg, Germany (Section 7); discussion and conclusions follow subsequently in Section 8.

2. Governing equations

The governing equations utilized in this study are based of the Boussinesq-type concept presented in Nwogu (1993), who improved the accuracy of linear dispersion through a Taylor series expansion retaining terms of the order of $O(\varepsilon, \mu^2)$, where $\varepsilon = a_0/h_0$ and $\mu = h_0/L_0$ define the non-dimensional parameters with respect to the order of nonlinearity and frequency dispersion and a_0 is the deep water wave amplitude. Nwogu (1993) introduced a variable reference depth (z_α) for evaluation of the horizontal velocities that is optimized for best agreement with a Padé [2/2] expansion in kh of the Airy dispersion relation.

The long-established equations by Nwogu (1993) contain a continuity equation and two momentum equations. Let ε and μ denote the nonlinear and dispersion parameters. Based on the fundamental assumptions of small amplitude and long period waves ($\varepsilon^2 \ll 1$, $\mu^2 \ll 1$) and in vector notation the equations read as

$$\eta_t + \nabla[(h+\eta)\mathbf{U}] + \nabla\cdot\left\{\left(\frac{z_\alpha^2}{2} - \frac{h^2}{6}\right)h\nabla(\nabla\cdot\mathbf{U}) + \left(z_\alpha + \frac{h}{2}\right)h\nabla[\nabla\cdot(h\mathbf{U})]\right\} = 0 \tag{1}$$

$$\mathbf{U}_t + \mathbf{U}(\nabla\cdot\mathbf{U}) + g\nabla\eta + \left\{\frac{z_\alpha^2}{2}\nabla(\nabla\cdot\mathbf{U}) + z_\alpha\nabla[\nabla\cdot(h\mathbf{U})]\right\}_t = 0 \tag{2}$$

The reference depth z_α is the vertical position within the still water column h, at which the velocities are evaluated. It is just below mid depth and varies linearly with the bathymetry. The governing equations exhibit good dispersion accuracy up to $kh \approx \pi$; for $kh > \pi$ ($k = 2\pi/L$) the error increases positively, i.e. the wavelength (L) is then overestimated. The equations' properties are very sensitive to the position of the reference depth (e.g. see Fig. 5 in Roeber et al., 2010). Generally, a choice of z_α closer to the free surface reduces the celerity error for short waves and vice versa. Since the position of z_α affects both linear and nonlinear wave components, it is important to find the best match between frequency dispersion and shoaling properties. So far, most studies have used values around $z_\alpha = -0.53h$ as initially proposed by Nwogu (1993). Roeber and Cheung (2012) proposed a value of $z_\alpha = -0.5208h$ to focus on shorter waves over the range of $\pi < kh < 2\pi$.

Recently, Simarro et al. (2013) recommended a value of $z_\alpha = -0.55502h$ as a better compromise between linear dispersion and shoaling properties. This z_α level is significantly lower than previously suggested values. Despite the larger error in frequency dispersion for individual waves of $kh > \pi$, $z_\alpha = -0.55502h$ targets the nonlinear energy transfer (shoaling properties) of an entire wave spectrum over irregular bathymetry. However, with focus on predominantly idealistic flat bed conditions and relatively short waves, the results in this study are based on $z_\alpha = -0.5208h$ as mentioned in Roeber and Cheung (2012).

Depth-integrated equations, which include non-hydrostatic properties, such as Boussinesq-type formulations were developed to handle nearshore processes in the subcritical as well as the supercritical regime. Toro (2009) demonstrated that the classical Shallow Water Equations cater to Finite Volume schemes, if the formulation is based on conserved variables. Roeber et al. (2010) adopted this concept and expressed the transported variables of the equations of Nwogu (1993) as conserved quantities. Defining the following variables such as H being total water depth, η representing the free surface elevation, ρ the water density, (u, v) as horizontal flow velocities in x and y directions, and with a stationary bathymetry, i.e. $h_t = 0$, the continuity equation can be readily expressed in terms of H in lieu of η. In differential form we get

$$H_t + (Hu)_x + (Hv)_y + \psi_C + \psi_{wm} = 0. \tag{3}$$

with ψ_C denoting the dispersion terms of the continuity equation as

$$\begin{aligned}\psi_C = &\left[\left(\frac{z_\alpha^2}{2} - \frac{h^2}{6}\right)h\left(u_{xx} + v_{xy}\right) + \left(z_\alpha + \frac{h}{2}\right)h\left((hu)_{xx} + (hv)_{xy}\right)\right]_x \\ &+\left[\left(\frac{z_\alpha^2}{2} - \frac{h^2}{6}\right)h\left(u_{xy} + v_{yy}\right) + \left(z_\alpha + \frac{h}{2}\right)h\left((hu)_{xy} + (hv)_{yy}\right)\right]_y\end{aligned} \tag{4}$$

Here, ψ_{wm} is a mass source term for the generation of spectral waves (shown for the sake of completeness). The momentum equations with conserved variables, Hu and Hv, arise from Equation (2) after pre-multiplication with H in combination with the continuity Equation (1), which is pre-multiplied by u and v respectively as

$$\begin{aligned}&(Hu)_t + H\left\{\frac{z_\alpha^2}{2}\left[u_{xx} + v_{xy}\right] + z_\alpha\left[(hu)_{xx} + (hv)_{xy}\right]\right\}_t \\ &\quad + \left(Hu^2\right)_x + (Huv)_y + gH\eta_x \\ &\quad + u\psi_C + H\tau_1 - H\left(\frac{\psi_S}{\rho}\right)_x = 0\end{aligned} \tag{5}$$

and

$$\begin{aligned}&(Hv)_t + H\left\{\frac{z_\alpha^2}{2}\left[u_{xy} + v_{yy}\right] + z_\alpha\left[(hu)_{xy} + (hv)_{yy}\right]\right\}_t \\ &+\left(Hv^2\right)_y + (Hvu)_x + gH\eta_y \\ &+v\psi_C + H\tau_2 - H\left(\frac{\psi_S}{\rho}\right)_y = 0.\end{aligned} \tag{6}$$

τ_1 and τ_2 denote the frictional drag terms based on a material or surface property associated with Manning's roughness n as

$$\begin{aligned}\tau_1 &= gn^2H^{-2/3}u\sqrt{u^2+v^2},\\ \tau_2 &= gn^2H^{-2/3}v\sqrt{u^2+v^2}.\end{aligned} \tag{7}$$

It should be noted that the hydrostatic NLSWE in conserved variable form are a complete subset of this Boussinesq-type equation (second line of Equations (5) and (6)).

The dispersion terms present a challenge to the time integration of the momentum equations. These terms are

$$\begin{aligned}&H\left\{\frac{z_\alpha^2}{2}\left[u_{xx}+v_{xy}\right]+z_\alpha\left[(hu)_{xx}+(hv)_{xy}\right]\right\}_t,\\ &H\left\{\frac{z_\alpha^2}{2}\left[u_{xy}+v_{yy}\right]+z_\alpha\left[(hu)_{xy}+(hv)_{yy}\right]\right\}_t.\end{aligned} \tag{8}$$

In contrast to the hydrostatic local acceleration terms, $(Hu)_t$ and $(Hv)_t$ of the NLSWE, where momentum is transported in time, the temporal derivative only affects the velocity components of the additional dispersive terms. For consistent incorporation of momentum in all terms of Equation (8), reorganization of the non-hydrostatic contribution through a simple product rule expansion leads to

$$\begin{aligned}&H\left\{\frac{z_\alpha^2}{2}\left[u_{xx}+v_{xy}\right]+z_\alpha\left[(hu)_{xx}+(hv)_{xy}\right]\right\}_t\\ &=\left\{H\frac{z_\alpha^2}{2}\left[u_{xx}+v_{xy}\right]+Hz_\alpha\left[(hu)_{xx}+(hv)_{xy}\right]\right\}_t\\ &-H_t\left\{\frac{z_\alpha^2}{2}\left[u_{xx}+v_{xy}\right]+z_\alpha\left[(hu)_{xx}+(hv)_{xy}\right]\right\}\end{aligned} \tag{9}$$

and

$$\begin{aligned}&H\left\{\frac{z_\alpha^2}{2}\left[u_{xy}+v_{yy}\right]+z_\alpha\left[(hu)_{xy}+(hv)_{yy}\right]\right\}_t\\ &=\left\{H\frac{z_\alpha^2}{2}\left[u_{xy}+v_{yy}\right]+Hz_\alpha\left[(hu)_{xy}+(hv)_{yy}\right]\right\}_t\\ &-H_t\left\{\frac{z_\alpha^2}{2}\left[u_{xy}+v_{yy}\right]+z_\alpha\left[(hu)_{xy}+(hv)_{yy}\right]\right\}\end{aligned} \tag{10}$$

Based on the explicit nature of the continuity equation, H_t is directly obtained from the flux and dispersion terms of Equation (3) as

$$-H_t=(Hu)_x+(Hv)_y+\psi_C. \tag{11}$$

The terms with second order xx or yy derivatives in Equations (9) and (10) can be isolated and grouped with the local acceleration term into evolution variables P and Q as

$$\begin{aligned}P&=(Hu)_t+\left[0.5z_\alpha^2Hu_{xx}\right]_t+\left[z_\alpha H(hu)_{xx}\right]_t\\ Q&=(Hv)_t+\left[0.5z_\alpha^2Hv_{yy}\right]_t+\left[z_\alpha H(hv)_{yy}\right]_t.\end{aligned} \tag{12}$$

The remaining terms from the product rule expansion of Equations (9) and (10), which are not used in Equation (12), are multiplied by Equation (11) and grouped together as

$$\begin{aligned}\psi_P&=\frac{z_\alpha^2}{2}u_{xx}+z_\alpha(hu)_{xx}\\ \psi_Q&=\frac{z_\alpha^2}{2}v_{yy}+z_\alpha(hv)_{yy},\end{aligned} \tag{13}$$

It should be noted that most BTE contain this rather challenging structure of time-dependent terms. Other approaches, such as the dispersive Nonlinear Shallow Water Equations presented in Antuono et al. (2009) might cater more directly to Finite Volume schemes. The ship-borne waves are generated with spatially moving pressure disturbances, ψ_S, in Equations (5) and (6). The shape of the ship hull is predefined at the beginning of the computation. The generation of waves from the moving pressure terms can coincide with other wave generating functions, such as a wave maker source for spectral or monochromatic waves.

3. Numerical scheme

The present Boussinesq-type formulation, with the NLSWE as subset, caters to solutions based on conservative numerical methods. As in previous studies, BOSZ utilizes a combination of a Finite Volume scheme for the hydrostatic parts of the equations and a central differential Finite Difference scheme for the non-hydrostatic pressure correction terms. The Finite Volume scheme solves for the spatial gradients of the flux and bed slope terms based of a solution from the Harten-Lax-van Leer-Contact (HLLC) approximate Riemann solver at all cell interfaces. A two-dimensional limiting reconstruction method presented in Kim et al. (2008) provides the input variables for the Riemann solution at all sides of the grid cells. The 4th-order reconstruction approach is oscillation controlled and wave-number extended, which greatly reduces numerical diffusion.

The equations can be casted in conservative vector form as shown in Toro (2009).

$$\overrightarrow{\mathbf{U}}_t+\overrightarrow{\mathbf{F}(\mathbf{U})}_x+\overrightarrow{\mathbf{G}(\mathbf{U})}_y+\overrightarrow{\mathbf{S}(\mathbf{U})}=0, \tag{14}$$

of which the vectors, omitting indices, are

$$\begin{aligned}\overrightarrow{\mathbf{U}}&=\begin{bmatrix}H\\P\\Q\end{bmatrix}\quad \overrightarrow{\mathbf{F}(\mathbf{U})}=\begin{bmatrix}Hu\\Hu^2+\frac{1}{2}g\eta^2+g\eta h\\Huv\end{bmatrix}\\ \overrightarrow{\mathbf{G}(\mathbf{U})}&=\begin{bmatrix}Hv\\Hvu\\Hv^2+\frac{1}{2}g\eta^2+g\eta h\end{bmatrix}.\end{aligned} \tag{15}$$

The evolution variables P and Q contain several terms with mixed space and time derivatives as shown in Equation (12). The variables $\overrightarrow{\mathbf{F}(\mathbf{U})}$ and $\overrightarrow{\mathbf{G}(\mathbf{U})}$ contain the homogeneous portion of the NLSWE equations with expanded surface gradient terms that are solved with the Riemann solver-supported Finite Volume scheme. The local acceleration and source terms in Equation (14) are part of the Finite Difference scheme and given as

$$\overrightarrow{\mathbf{S}(\mathbf{U})}=\begin{bmatrix}\psi_C\\-g\eta h_x+u\psi_C-H_t\psi_P-H\psi_{P2}+H\tau_1-H(\psi_S/\rho)_x\\-g\eta h_y+v\psi_C-H_t\psi_Q-H\psi_{Q2}+H\tau_2-H(\psi_S/\rho)_y\end{bmatrix}. \tag{16}$$

The ψ_S-terms in (5), (6), and (16) describe the shape of a pressure disturbance to generate ship-borne waves. Even though the pressure field could take on a wide range of shapes, in this study we will use the formulations presented in Bayraktar and Beji (2013). Equation (17a) results in a hemispherical and Equation (17b) in an elongated, more ship like pressure distribution. The two shape types are spatially defined as

$$(\psi_S)_{i,j}=D_p\sqrt{1-\left(x_i^2+y_j^2\right)/r^2} \tag{17a}$$

$$(\psi_S)_{i,j}=D_p\left[1-c_L\left(x_i/L_p\right)^4\right]\left[1-c_B\left(y_j/B_p\right)^2\right]e^{-a\left(y_j/B_p\right)^2} \tag{17b}$$

Here, L_p, B_p, D_p denote the length, breadth (measured from the longitudinal center axis), and draft of the pressure, r is the radius of the hemispherical shape, and a, λ_L and λ_B are form parameters set to 16, 2,

and 16, resulting in a slender body. In Equations (17a) and (17b), D_p denotes as $D_s \cdot 10^5$ with D_s as the corresponding ship draft multiplied where $1\ \text{bar} = 10^5\ \text{N/m}^2 = 10^5\ \text{kg/ms}^2$, resulting in a water level depression of $\eta = D_s$. Fig. 1 shows a non-moving, steady pressure term with $D_p = D_s = 2.5$ m and its influence on η. In this initial test, the pressure size is $L_p = B_p = 20$ m, while the grid spacing is $\Delta x = \Delta y = 1$ m. Fig. 1a shows, how the pressure term is introduced onto the water surface with a speed of $\tanh(0.25 t_{mod}) \cdot \psi_S$ in this test, where $t_{mod} = 1$ s is the model time. The waves generated radiate off the pressure perturbation with rotational symmetry, which is in accordance to Wei and Kirby (1995) and Bayraktar and Beji (2013). The reproduction of the stationary pressure distribution on the water surface is an important prerequisite to study the moving pressure perturbation in the following. Both Fig. 1a and b show the footprint of the hemispherical pressure form, which remains constant in location on the water surface. In Fig. 1b, at $t_{mod} = 10$ s, the ramping function results in $\tanh(2.5) \cdot \psi_S = 0.987 \psi_S$, while the actual $\eta_{min.}$ in the model is $0.985 D_p$. The pressure perturbation is therefore considered to be implemented correctly. Thus, ship length and breadth as well as draft and velocity L_s, B_s, D_s and c_S will be used synonymously with the pressure length, width, magnitude and velocity. Likewise, BOSZ is able to produce the non-stationary case presented by the aforementioned authors, which comprises a pressure term quickly released after a few milliseconds. The result is an oscillation of η, similar to an object thrown into the water (not shown here for brevity). Depending on the forward speed c_S of the ship, the location of the pressure disturbances moves with time. Due to the discrete nature of the numerical grid, the position of the disturbance is bound to the grid cells to preserve the overall pressure quantity.

BOSZ includes total variation diminishing scheme (TVD) versions of the second, third, and forth-order Runge Kutta time integration methods (Gottlieb et al., 2001). These schemes favor the use of a dynamically changing time step based on the overall flow field, since the higher-order accuracy is achieved throughout multiple evaluations of the equation per time step.

The evolution variables with combined flux and dispersion terms in (12) form tridiagonal linear systems of equations, which can be solved for the horizontal flow velocities u and v through an LU decomposition with data dependency in either the x or the y direction. This facilitates parallel computation as no iterative procedure is required. The upper, lower, and diagonal vectors of the sparse matrices can be pre-factored in the beginning of the computation and only have to be multiplied by a changing H in each Runge-Kutta step throughout the time integration procedure.

In addition, the momentum equations contain non-hydrostatic parts from the orthogonal velocity components with cross-space and time derivatives (see Equations (9) and (10)) that are treated separately. The xyt cross terms of (9) and (10) are repeated here as

$$\psi_{P2} = \frac{z_\alpha^2}{2} v_{xyt} + z_\alpha (hv)_{xyt} \tag{18}$$

and

$$\psi_{Q2} = \frac{z_\alpha^2}{2} u_{xyt} + z_\alpha (hu)_{xyt} \tag{19}$$

and they are evaluated with first-order upwind discretization of the u_t and v_t time-derivatives based on stored variables from the current and the previous time steps. The Courant number is set to constant 0.5 for all tests in this study. The time step size is calculated in the beginning of each time step and it can vary according to the flow conditions so that the Courant constraint is never violated.

4. Model setup

As a first step, a sensitivity test is required to narrow down an optimal model setup with respect to domain and grid size as well as wave gauge positions. Accordingly, the rectangular domain, which is depicted in Fig. 2, provides the test bed (virtual basin) to investigate optimal balance between accuracy and computational cost. This was accomplished by increasing the mesh resolution in subsequent steps. The optimum meshsize is then used to validate the pressure term implementation as well as to test sensitivity of the pressure term parameters. The identical computational domain is also used in the validation runs, outlined in Section 5. The computational domain extends 840 m in x-direction and 408 m in y-direction measured from the lower left corner (0/0). The depth of the virtual basin is $h = 5$ m. The ship track approximated by a moving pressure field approach follows the center axis of the computational domain parallel to the long domain axis, starting at coordinate (36/204) to coordinate (804/204). To accomplish open basin conditions, the above described domain is enclosed by a sponge layer. It effectively absorbs wave energy propagating outwards of the domain and prevents the creation of reflective waves at the boundaries. This non-reflective, buffer zone-type boundary condition extends over 30 cells (30 m) at each side of the domain. The wave gauges A-F in the domain were positioned to be affected by both the wake behind the pressure term and a fully evolved wave field: In Fig. 2, the dark shaded area shows the coverage of the Kelvin wedge with a half-angle of $\theta_K = \arcsin 1/3$, while the lighter shaded part is the area covered by the vessel wake in depth-limited waters. A fully evolved wave field requires a couple of seconds ramping time after the pressure term departs, meaning that the gauges

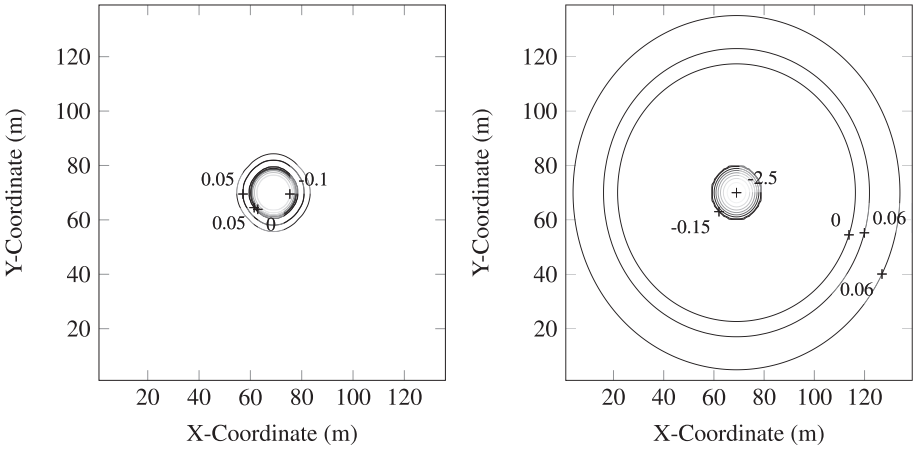

(a) Wave pattern after 1 s.

(b) Wave pattern after 10 s

Fig. 1. Contour plots of η for a non-moving, steady hemispherical pressure field with $D_p = D_s = 2.5$ m, resulting in a ring wave pattern.

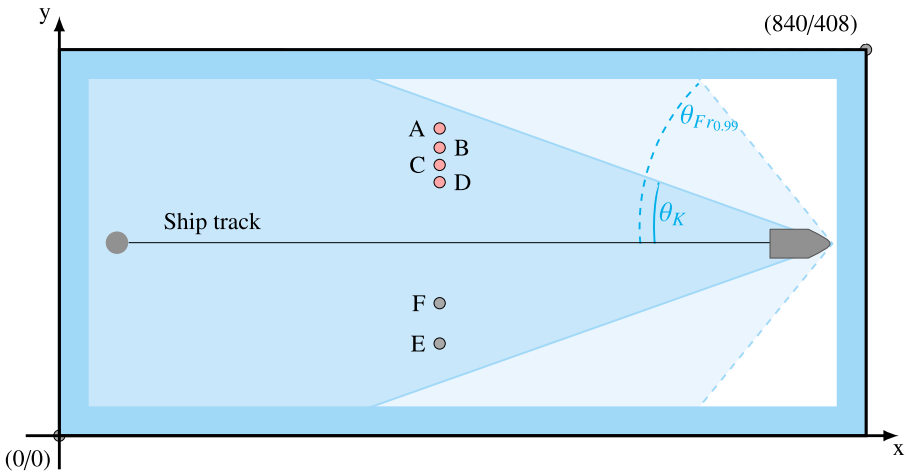

Fig. 2. The computation domain is 840 m·408 m large and contains six gauges. The domain is surrounded by a sponge layer and the shaded areas show the formation of the Kelvin wedge or as Fr_h increases its depth-limited equivalent according to Havelock (1908).

should not be positioned too close to the starting point. Table 1 lists the positions of the virtual wave gauges A-F. In the following, this study considers shape and wave height H_{lw} of the leading wave, but also the wave height of the largest wave H_{max} in the generated wave train. This maximum wave height varies throughout the wave train with increasing distance from the sailing line, therefore some of the below shown experimental analysis will regard the maximum water level elevation η_{max} in the wave train, analogue to the maximum wave height H_m as suggested by Sorensen (1997).

The calibration runs employ a slender pressure type as described in Bayraktar and Beji (2013) with both beam B and length L being $B = L = 6$ m and a draft of 1 m. The volume and dimension of the pressure form require special attention, as they must not change when refining the grid. The pressure disturbance is traveling at $Fr_h = 1.2$. The time series for each grid size in Fig. 3 shows, that numerical diffusion leads to a visible underestimation of H_{lw} for grid sizes of $\Delta x, \Delta y > 1.0$ m. As the bow wave has similar characteristics of a soliton with a theoretically infinite wave length, H_{lw} in this study is the height of the leading wave, measured from draw-down to stern wave. Table 2 gives an overview of the convergence runs and contains information on the grid size in each direction, the respective amount of total grid cells in the domain as well as the computation time t_{comp}. Additionally, Table 2 combines this information with H_{lw} from Fig. 3 and ΔH_{lw} being the improvement of H_{lw} towards the former grid size. Contrary to the leading first and second waves, which showed excellent agreement between the two highest resolutions, the trailing wave system shows less favorable agreement attributed to numerical diffusion. With this study aiming on replicating leading ship waves, convergence of the solution is reached at 1.0 m grid spacing. Albeit the resolution of the secondary wave system is finer for a grid size of 0.75 m compared to a grid size of 1.0 m, the grid refinement also results in a duplication in computation time, whereas the determining parameter H_{lw} improves only in the order of millimeters. The ideal grid size for this study is therefore chosen to be $\Delta x, \Delta y = 1.0$ m.

On a secondary note, the computation time varies significantly between the second-, third-, and forth-order strong stability-preserving (SSP) time integration schemes (Gottlieb et al., 2001). The multi-step methods require two, three, or four evaluations of the governing equation per time step and hence, the third-order method takes about 50% more computation time and the forth-order method requires about twice the effort compared to the second-order method assuming the same Courant number constraint for all methods. Only very little difference was found between third- and fourth-order SSP Runge-Kutta-Scheme. Compared with the second-order scheme, the third-order SSP scheme shows marginally less diffusion, and, as a conservative approach, is used in the following runs. Additional computation time could be saved by considering only one side of the symmetric ship wake, yet in the present study, gauges D to F are set up to both sides of the track to cross-validate the results.

Table 1
Positions of the wave gauges.

Gauge	X-Coordinate	Y-Coordinate
Position A	396	306
Position B	396	300
Position C	396	282
Position D	396	264
Position E	396	138
Position F	396	96

5. Validation

Next, the pressure term implementation in BOSZ is validated by varying the vessel speed and studying the response of the wake angle with the analytical solutions derived by Lord Kelvin (William Thomson) (1887) and Havelock (1908). (An explanation will follow, however Soomere (2007) illustrates this very well in a broader context.) Lord Kelvin (William Thomson) (1887) derived the half-angle θ_K created by the intersection of the transverse and divergent waves analytically. He compared the phase celerity $c_{ph} = c_S \cos\theta_K$ of the waves, traveling in the cusp line, with their group velocity c_g. From $c_{ph} = 2c_g$ in infinite water depths, Lord Kelvin (William Thomson) (1887) derived $\sin\theta_K = 1/3 = 19.47°$ for any moving object in deep water. According to the findings of Lord Kelvin (William Thomson) (1887), the wake for deep water conditions is also known as Kelvin wake. The Kelvin wedge behind a moving object θ_K remains constant for $Fr_h \leq 0.55 - 0.7$, where the deep water limit $kh \geq \pi$ is valid for $Fr_h \leq 0.687$ (Soomere, 2007). Havelock (1908) enhanced Lord Kelvin's analytical formulation to depth limited waters by reformulating the Froude number Fr_h in the subcritical range with p and under the assumption of a moving point source:

$$p = \frac{1}{Fr_h^2} = \frac{gh}{c_S^2} \tag{20}$$

and iterates the associated water depth kh with the following relation:

$$\frac{\tanh kh}{kh} = \frac{2}{p(3-n)} \tag{21}$$

where

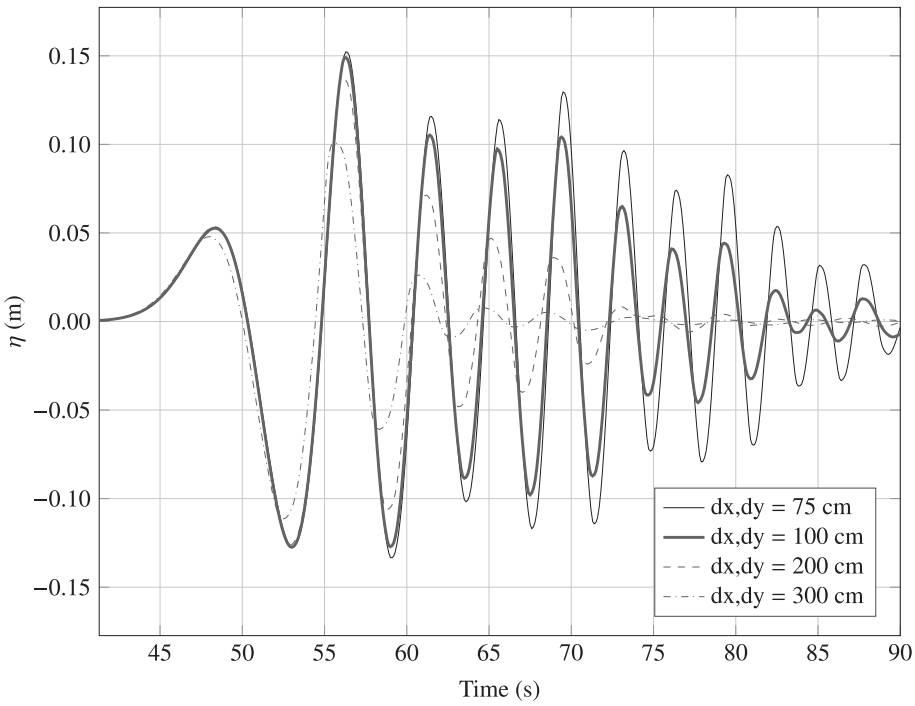

Fig. 3. Wave record at position A for several grid sizes, showing the convergence of BOSZ for ship waves. With respect to accuracy and efficiency, a grid size of 100 cm is used for the subsequent tests.

Table 2
Model performance due to grid refinements on a cluster containing 20 processors with a clock speed of 2.00 GHz each.

$\Delta x, \Delta y$ (m)	Grid cells (–)	t_{comp} (s)	H_{hw} (m)	ΔH_{hw} (m)
3	38,080	106	0.212	(–)
2	85,680	272	0.263	0.051
1	342,720	1150	0.276	0.013
0.75	609,280	2138	0.280	0.003

$$n = \frac{2kh}{\sinh 2kh} \tag{22}$$

The corresponding wake angle θ_K for depth limited waters can then be determined with n and p for subcritical and supercritical speeds:

$$\theta_K = \arccos\left(\frac{\sqrt{8(1-n)}}{(3-n)}\right) \quad \text{if } Fr_h \leq 1 \tag{23a}$$

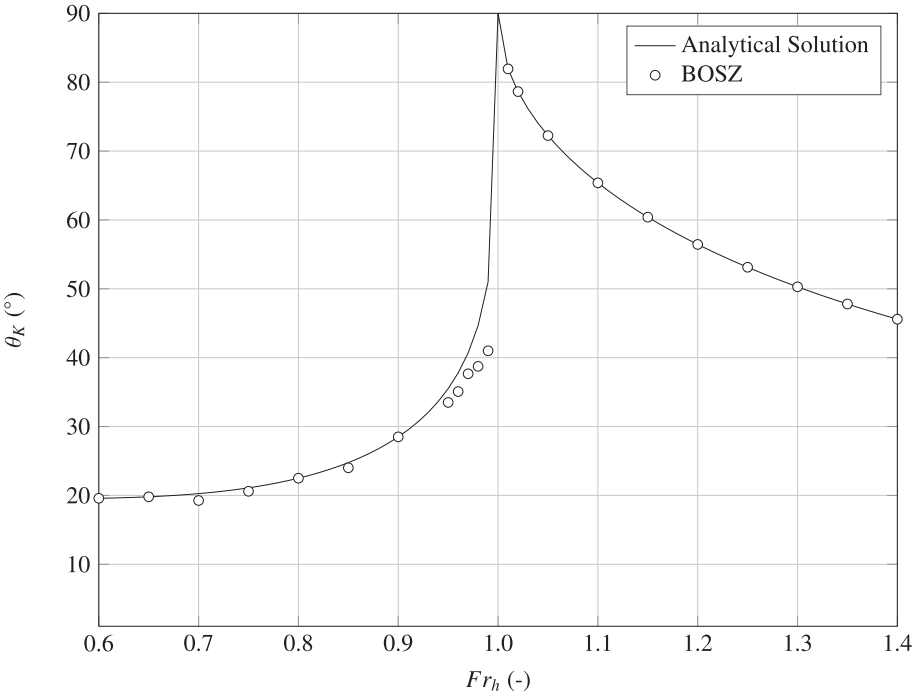

Fig. 4. The black line shows the analytical solution of Havelock (1908) for half angles of ship wakes in depth limited waters. The half angles computed by BOSZ are plotted as circles.

$$\theta_K = \arcsin\left(\sqrt{p}\right) \quad \text{if} \quad Fr_h > 1 \tag{23b}$$

Here, the reproduction of the analytical solution of the wake angle serves to evaluate the applied numerical schemes. This exercise can easily be used as benchmarking exercise for any CFD model. The results will give information on how well the velocity components u and v of the governing equations are solved by the chosen numerical implementation. However, this gives no direct information about the quality of the computed water level elevation η.

Fig. 4 contains the results for Equation (23a) as well as for the numerical computations in the range of $Fr_h = 0.6 - 1.4$. Roeber and Cheung (2012) optimized BOSZ to compute the wave celerity with an error smaller than 4% at $kh = 5$. With the deep water limit $kh \geq \pi$ at $Fr_h \leq 0.687$ (Soomere, 2007), $kh = 5$ is equivalent to $Fr_h = 0.432$ and thus, the chosen range is well within the model's applicability. According to Zhu et al. (2015), the angle of the wake pattern are related to the cusp angle for $Fr_h \leq 1$ and the asymptote angle for $Fr_h \geq 1$. Fig. 5 shows the wave pattern in plane view calculated by the model and contains the analytical solution according to Havelock (1908). The runs use a slender body pressure type with 12.0 m length, 6.0 m beam and 2.0 m draft. Comparing the approach of Havelock (1908) with the computed wedge is a keystone validation step for ship-borne waves in numerical models, as it shows the model's ability to recreate the wave pattern. Hydraulic model tests (see for example Johnson, 1957) can be reproduced quite well by depth-averaged, phase-resolving wave models (see Liu and Wu, 2004; Dam et al., 2006; Bayraktar and Beji, 2013). Fig. 4 as well as 5 show, that BOSZ represents the analytical solution very well, albeit having a slight tendency to under-predict wave angles between $0.9 < Fr_h < 1$. Yet deviations of wake angles are likely for subcritical and especially near-critical Froude numbers and are in accordance with other studies (e.g., Bayraktar and Beji, 2013).

Zhu et al. (2015) study the wake pattern in more detail analytically and by regarding the correlation between transverse and divergent waves. With this they find a correlation for the composition of the wake pattern when considering different length-based Froude numbers. Zhu et al. (2015) associate $Fr_{L,min}$ and $Fr_{L,cusp}$ with the smallest wavenumber and the cusp wavenumber found in the pattern, as well as the critical Froude number $Fr_{L,critic}$, corresponding to water depths where Fr_h is at unity. The wake pattern shown in Figs. 5 and 6b correlate with the findings of Zhu et al. (2015). The computations shown in Fig. 6b use $Fr_h = 0.60$ and are carried out with the same setup than those used for results presented in Fig. 5. For pressure term dimensions of $L_s = 6.0$ m and $h = 5.0$ m, depth-based Froude numbers $Fr_h = 0.60$ and $Fr_h = 0.70$ correlate to $Fr_L = 0.55$ and $Fr_L = 0.64$ respectively. The composition of the wake pattern in Figs. 5 and 6b follow the findings of Zhu et al. (2015), when inserted into Fig. 6a, which is transverse waves are dominant in the wake pattern of $Fr_h = 0.60$ (regime 2), while divergent waves become significant for $Fr_h = 0.70$, Fig. 5a (regime 3). The significance of transverse waves in the wake pattern decreases even more when Fr_h increases, as shown for $Fr_h = 0.95$ in Fig. 5b. As per definition of Fr_h, no transverse waves are found in the wake of supercritical depth-based Froude numbers which is exemplified by computations for $Fr_h = 1.10$ and $Fr_h = 1.40$, depicted in Fig. 5 (regime 4).

A realistic representation of the wake angle and pattern should be achieved, however the most common purpose of wave models is to

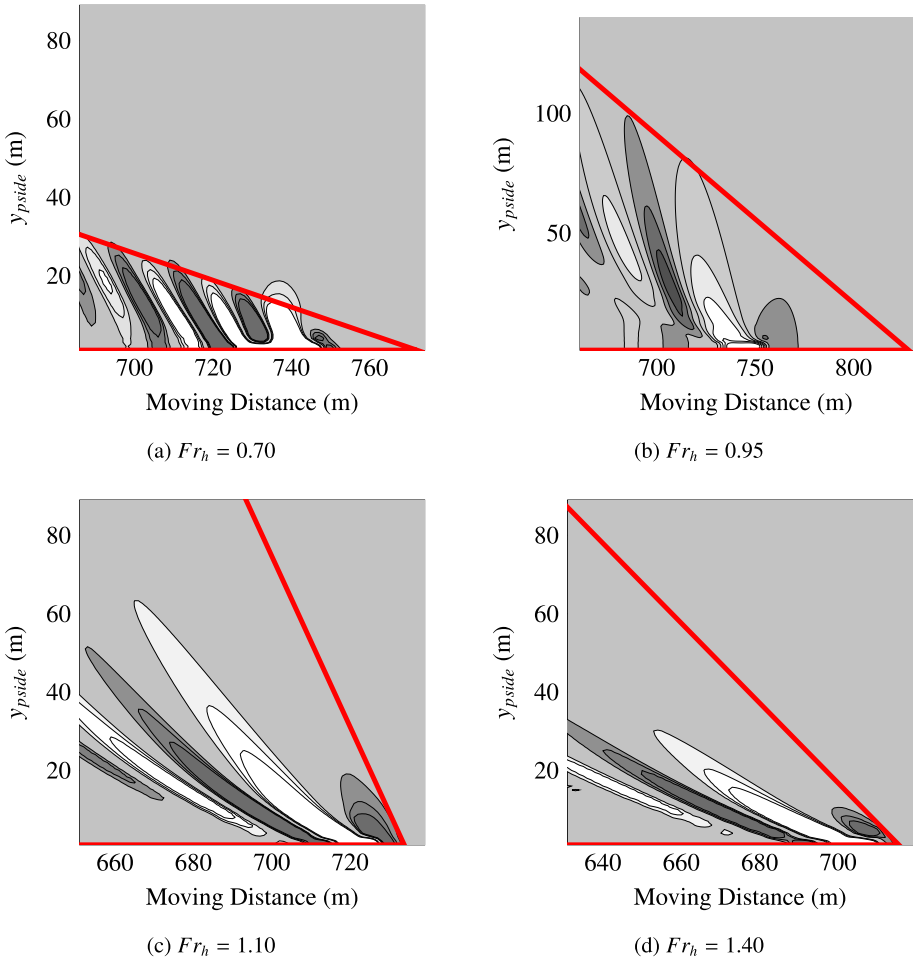

Fig. 5. Computed wave patterns from BOSZ and half angles (red lines) according to Havelock (1908) for $Fr_h = 0.7$, 0.95, 1.1 and 1.4. (For interpretation of the references to colour in this figure legend, the reader is referred to the web version of this article.)

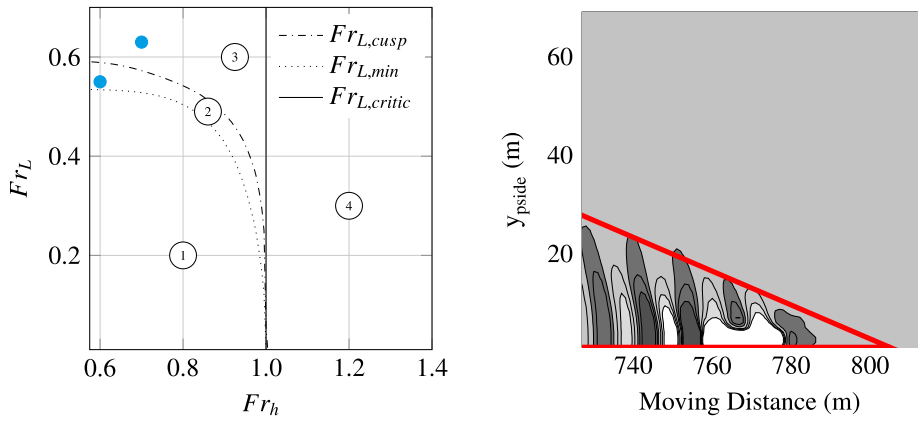

(a) Regimes for different wave pattern, adapted from Zhu et al. (2015)

(b) Fr_h = 0.60

Fig. 6. Zhu et al. (2015) presented four wake regimes for varying Froude numbers Fr_h and Fr_L: 1. no primary wave interference, transverse waves exist, 2. transverse waves interference, 3. divergent waves interference, transverse waves exist 4. divergent waves interference, no transverse waves. The wave pattern for $Fr_h = 0.60$ with $Fr_L = 0.55$ for the present setup and $Fr_h = 0.70$ with $Fr_L = 0.64$ from Fig. 5a are marked with blue dots. When regarding both patterns of $Fr_h = 0.60$ and $Fr_h = 0.70$, the presence of transverse waves varies visibly. (For interpretation of the references to colour in this figure legend, the reader is referred to the web version of this article.)

determine wave parameters like wave height and wave period. Because the pressure term implementation is only a simplified solution to the fluid-body interaction problem around the vessel's hull, it is necessary to determine at what distance the implementation produces typical results accurately. Fang et al. (2011) give a rough estimation, by defining the far field of a vessel for distances of $L_{ff} \gg c_S^2/g$ with L_{ff} =7.2 m in the present case.

Fig. 7 provides detailed information of the maximum free surface elevation η_{max} lateral to a slender-body type pressure distribution with 12.0 m length, 6.0 m beam and 2.0 m draft. Fig. 7 shows η_{max} portside of the pressure term at each grid cell over a distance of y_{pside} =300.0 m. For similar field measurements and physical experiments, Johnson (1957), Nece et al. (1985) and Macfarlane (2012) used a regression analysis for their scattered data and found a strictly monotone and exponential decreasing function for η_{max}. BOSZ can almost exactly reproduce the behavior of these findings. Only a dip at around ~ 20−40 m distance to the pressure disturbance is not covered by the regression functions, but are in the range of the scattered data. Altogether, the computation in Fig. 7 is in good accordance with the other studies, but should be backed up by physical models to increase confidence.

The most dynamic response of wave height is found for varying Fr_h. Fig. 8 shows η_{max} at wave gauge A to D. The behavior of η_{max} vs. Fr_h is analogue to the behavior of θ_K vs. Fr_h, in which η increases for sub- and near-critical Froude numbers until it decreases for super-critical Froude numbers. Fig. 8 shows that the model reproduces this trend very well. For positions with $y_{dist} \geq$80.0 m, the highest $\eta_{max.}$ in Fig. 8 is at $Fr_h = 0.96$. This is in accordance with the findings in Johnson (1957), who recorded both η_{max} in a small scale physical model and in Dam et al. (2006), who also enhanced BTE with a pressure term. The computations of Dam et al. (2006) yielded in a very similar evolution for $\eta_{max.}$ over Fr_h with max.

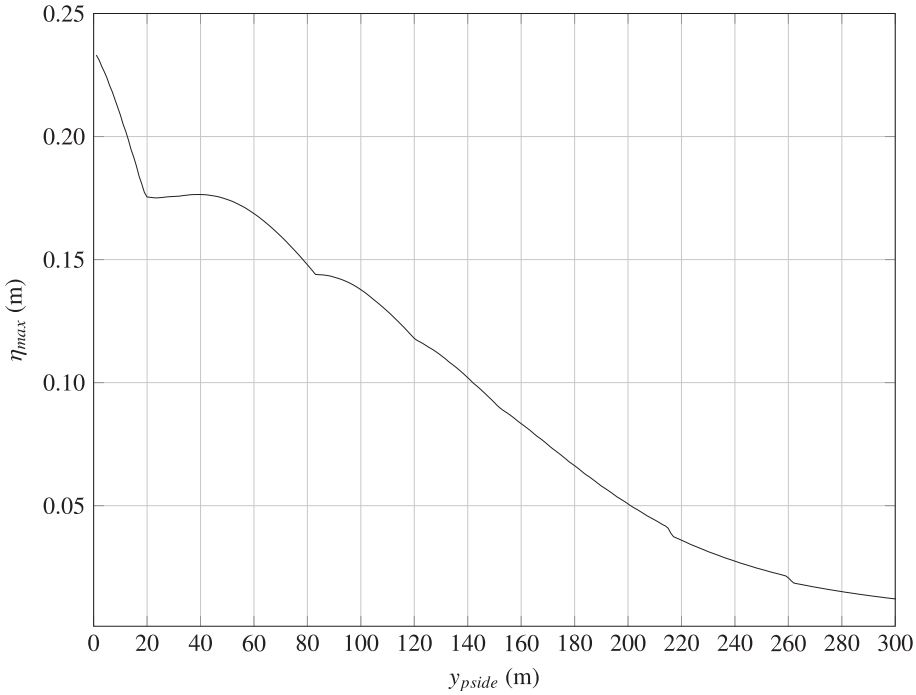

Fig. 7. Evolution of η_{max}, measured along a trajectory lateral to the pressure term of 300 m away from the outer hull.

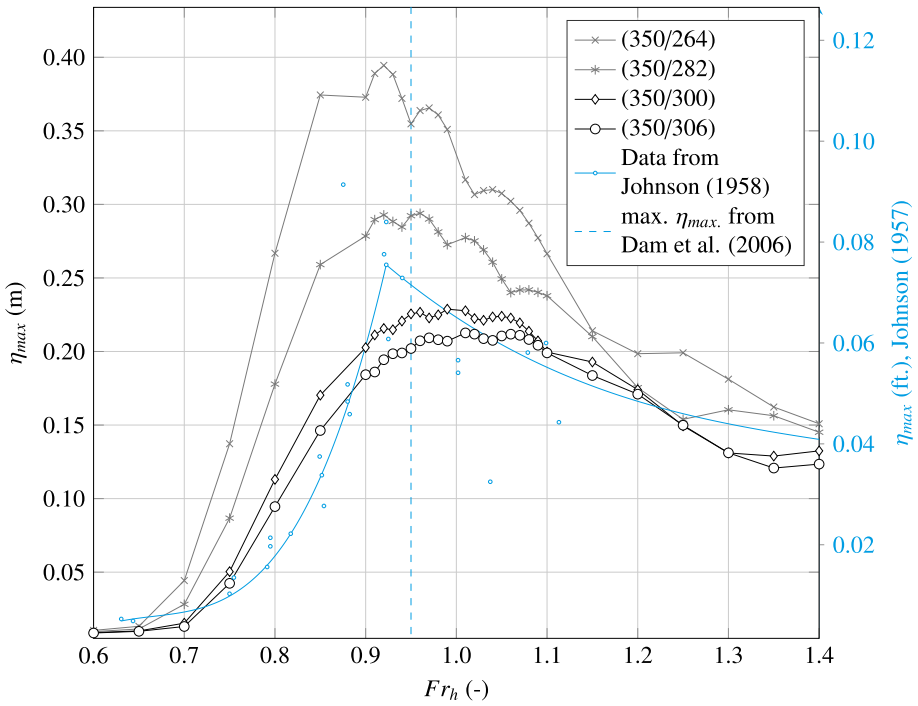

Fig. 8. Evolution of η_{max} throughout the domain for different Froude numbers Fr_h. The values were taken from gauges A to D while the blue line represent the laboratory data from Johnson (1957). The graphs show maximum wave heights at virtual wave gauge positions (X/Y) in the coordinate system presented in Fig. 2. The ship's sailing path is along $y = 204$. (For interpretation of the references to colour in this figure legend, the reader is referred to the web version of this article.)

$\eta_{max.}$ to be at $Fr_h \approx 0.96$. For wave gauge A though, which is closest to the sailing line, BOSZ tends to yield higher than expected $\eta_{max.}$ between $Fr_h = 0.85$ and $Fr_h = 0.94$ when compared to the findings in Johnson (1957) and Dam et al. (2006). In the current case, $\eta_{max.}$ is typically in the secondary wave system. Macfarlane (2012) measured the wave height obtained in an experiment close to the ship with $y_{pside}/L = \mathcal{O}(1)$ and divided the wave train in three sections: the primary wave system consistent of bow and leading wave, as well as two sections in the secondary wave system. For the section being equivalent to $\eta_{max.}$ in Fig. 8, Macfarlane (2012) calculated the highest wave being close to $Fr_h = 0.85 \pm 0.05$, which is similar to our results.

As the maximum water level elevation η_{max} varies throughout the wave train for different Fr_h, the according wave periods $T_{\eta max.}$ are not representative when compared to each other. However the wave periods T_{lw} of the leading wave H_{lw} can be compared to each other. T_{lw} for different Froude numbers Fr_h are displayed in Fig. 9 and show a

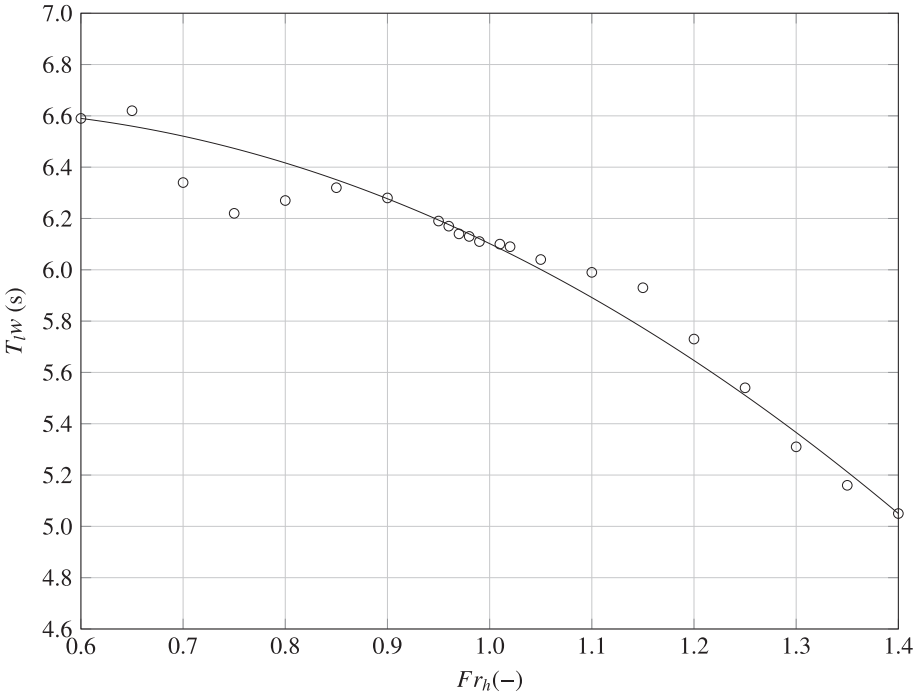

Fig. 9. Evolution of the leading wave period T_{lw} (circles) over the Froude number Fr_h. The line approximates the values with a cubic spline interpolation.

decreasing trend as Fr_h increases. While a direct comparison of the numerical results with literature data was difficult due to scarce data, evidence for a correct range of ship wave periods arises from other empirical research. Curtiss et al. (2009) report ship wave periods as generated by a Seattle bound car ferry to range between 3.0 s and 6.0 s based on field measurements. In the context of container ships, some larger wake periods were found, ranging between 6.0 m and 17 m (Houser, 2010); yet, none of these empirical data was related to parameters hinting at ship velocities or detailed hull geometries that caused the waves in the first place. In the present study, vessel wave periods vary between 5.05 s and 6.59 s. While the wave periods obtained by numerical model appear to reside in the correct range given the field evidence, it seems necessary to strive for additional benchmark tests in unbiased laboratory conditions to supplement future modeling.

6. Discussion

Next, a discussion is provided as to how different pressure term shapes of different aspect ratios contribute to the resulting wave properties in the far field. This question is important to practitioners and researchers alike. BAW (2010), Sorensen (1997) and Johnson (1957) have investigated how modifications of vessel dimensions affect the hydrodynamic response in the water body. Resulting parameterized approaches were often highly site-specific without providing guidance on the general wave properties yielded by specific ship hulls. To date it is yet not fully clear how pressure term dimensions in Boussinesq-type models affect the resulting wave systems in the surrounding domain.

BAW (2010) found typical relationships for wave height evolution to changes in vessel-representing pressure term length for either riverine waterways and channels or for fast boats, traveling at critical and supercritical speeds. In terms of vessel width and draft however, the evolution of wave heights was not yet explicitly studied. BAW (2010) defines an applicable speed regime for inland waterways and calculates wave heights by the use of form coefficients for some specific vessel types. Sorensen (1997) compared 9 methods, predicting wave height generated by vessels. The equations are based on results from physical models or field measures. Most of these approaches are based on very basic input parameters. This is why Sorensen (1997) finds only three of them being applicable in a more general form. The model of Gates and Herbich (1977) contains an indication of the bow angle at the water line as well as a hull coefficient, being a function of vessel speed and length. However the parameter is only defined for larger vessels. PIANC (1987) also define a form parameter, where Verhey and Bogaerts (1989) included a coefficient to account for the bow geometry, however this was coupled with a tuning coefficient. Weggel and Sorensen (1986) also incorporated the displacement volume of the vessel, but Sorensen (1997) criticize this model and describe the response of the model to the implementation of the direct vessel hull form as indirect and limited.

The influence of pressure term aspect ratios on resulting maximum wave heights at some distance of the sailing line are studied for various square pressure terms, modifying the aspect ratio either to the length-wise (L_0) or width-wise (W_0) direction, with the pressure term always moving in the direction of L. The initial square pressure surface with $L_0 = W_0$ =6.0 m for a constant grid size of $\Delta x = \Delta y$ =1.0 m is chosen. Firstly, aspect ratios in length-wise direction are step-wise increased to $L = 10{\cdot}L_0$, and in a second step, the width parameter are increased until it reaches 10 times the initial width while keeping the length constant. Each test is carried out for both sub- and supercritical conditions $(Fr_h = 0.85, 1.20)$; the model output is subsequently evaluated at a wave gauge located at 120.0 m+0.5W distance to the sailing line.

The investigated depth Froude numbers Fr_h show similar response to changes in pressure term length, as is shown in Fig. 10a. The computation addresses effects of superposing vessel waves, which are highest when the wave-generating ship length L_w is equal to half the length of the secondary waves. According to BAW (2010), this is given when $\pi c_S^2 g^{-1} \approx L_w$ with $L_w = \beta L_S$, where $\beta = 0.72$ is used for fast ships and $\beta = 0.90$ for common vessels (BAW, 2010). For the present setup, this corresponds to $4.2L_0$ for $Fr_h = 0.85$ and $5.2L_0$ for $Fr_h = 1.2$ Fig. 10a shows, that the model can recreate these values well, by having the largest η_{max} at $3.75L_0$ and $5L_0$ for $Fr_h = 0.85$ and $Fr_h = 1.2$ respectively. As stated by BAW (2010), the maximum surface elevation shifts to smaller ship lengths for lower velocities, which agrees well with the results shown in Fig. 10a.

As a variation, Fig. 10b plots the results as a function of the length Froude number $Fr_L = c_S/\sqrt{g{\cdot}L}$, being the vessel velocity to length-based celerity. It is often used for ship design purposes in naval architecture. In this framework, $Fr_L < 0.4 - 0.6$ results in the so-called *displacement mode*, while length Froude numbers $Fr_L > 1$ are called *planing*. The intermediate state between displacement and planing is *plowing* which applies for $0.4 - 0.6 < Fr_L < 1$.

The length Froude number explicitly contains effects of a hull's skin friction, and thus resistance of a ship's hull. In the present case, it is an important dimensionless number, because it qualitatively explains why some maximum surface elevations of generated ship waves are reached. It is assumed that increasing friction corresponds to the surrounding surface perturbation. Here, the highest waves are found around the

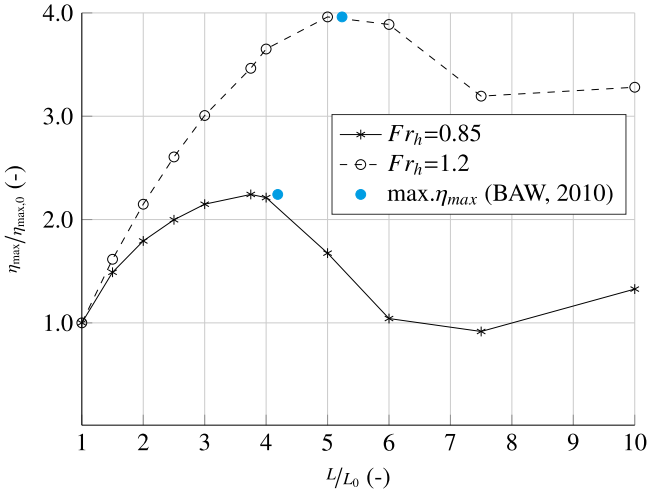

(a) Dimensionless maximum surface elevation as a function of the length aspect ratio L/L_0

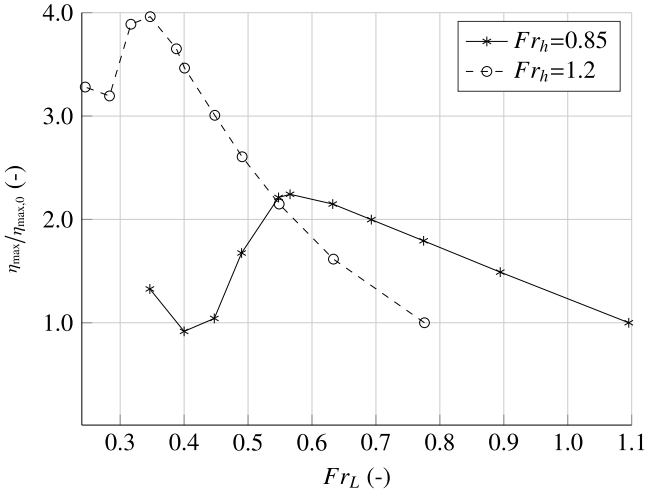

(b) Dimensionless maximum surface elevation as a function of the length Froude number.

Fig. 10. Maximum water level elevation η_{max} for different pressure term lengths, with an initial ship length $L_0 = 6.0$ m and a constant width $B_0 = 6.0$ m. The data is recorded at 120 m $+0.5B_0$ with respect to the sailing line.

transition of displacement to plowing, corresponding to $Fr_L = 0.35$ ($Fr_h = 0.85$) and $Fr_L = 0.57$ ($Fr_h = 1.2$) in Fig. 10b. These results qualitatively follow earlier findings presented by Sorensen (1973) and Wang and Zou (2008). The model does also shift the peak to smaller Fr_L for shallower waters, which agrees with results shown by Tarafder (2007).

Fig. 11 shows the effects of changing pressure term width for length Froude numbers between $Fr_L < 0.4 - 0.6$. Subcritical ranges are much more prone to changes in width, yielding an 10.2-fold increase of η_{max} as compared to a square pressure term (aspect ratio of unity). For the supercritical range, the maximum surface elevation increases by a factor of 3.24. Fig. 11 also shows, that η_{max} will decrease rapidly.

In order to address changes of pressure term's aspect ratio to resulting wave periods, Figs. 12 and 13 display wave records for different pressure aspect ratios. Table 3 contains the corresponding η_{max} for η/η_{max}. Fig. 12 shows, that wave periods differ to a minor extent for subcritical Froude numbers ($Fr_h = 0.85$). Yet, the pressure term with $L = 6L_0$ and $B = 1B_0$ shows more pronounced secondary waves than the remaining pressure terms. Wave periods for supercritical Froude numbers ($Fr_h = 1.20$), in Fig. 13 require a closer inspection, as the drawdown (trough) and leading wave superpose for pressure terms with $L = 10{\cdot}L_0$. Table 4 gives an overview of three sections in the wave train. Based on T_{lw}, Table 4 also contains the duration of the drawdown in front of the leading wave T_{dd}, as well as the wave followed by the leading wave T_{lw+1}. For supercritical speeds, more slender ships result in more complex wave trains, as the drawdown increases and superposes with the leading wave. As well, the primary wave system gains further complexity when the ship's width increases. However the resulting wave periods for T_{lw+1} remain almost equal for all tested pressure dimensions, showing that the wave period of the secondary wave system remains almost unaffected by the vessel's dimensions.

Eventually, the effect of different pressure term magnitudes was investigated for a slender pressure term of 24.0 m length and 8.0 m width. The pressure term's magnitude was thus varied between values of 0.1 m–3.0 m, using increments of $\Delta D_S = 0.1$. As shown in Fig. 14, the response of maximum free surface elevation η_{max} at some distance to the sailing line of the pressure term reveals a linear relationship to the pressure term. Although this characteristics could have been anticipated beforehand, it is nevertheless important to show as it allows modelers of practical problems to set specific wave heights at some point and study their effects on embankments or vegetation patches along a shoreline for predefined parameters.

7. Application

In order to test the model's applicability to real-world cases, a field site was chosen that exhibits significant loading from ship-induced waves. As the model's capabilities with regard to generating ship-like wave systems was assessed through academic test cases before, it subsequently needs to show its usefulness in such challenging environment. The harbor of Hamburg resides about 120 km upstream of the North Sea at the river Elbe; it faces high loads of ship traffic which essentially is a mixture of public transport fast ferries connecting both sides of the Elbe, tug boats used to operate container vessel arrival and departure as well as various other boat operations. The Hamburg Port Authority (HPA) is responsible for the harbor activities between the North Sea and Hamburg. HPA operates a wave gauge in the river Elbe in Nienstedten, Germany, close to Hamburg. It consists of an acoustic water level sensor, which measures the vertical distance between the water surface and the instrument's position. In order to yield reproducible, yet distinguishable ship-wave systems, a 19.6 m long and 5.1 m wide barge with a draft of 1.5 m sailed along a linear trajectory at predetermined vector along the wave gauge. The on-board Automatic Identification System (AIS) gave information about the ship's positional coordinates. The average deviation between the projected and estimated route was 1.60 m (standard deviation: 0.95 m). The wave-data of the gauge was recorded between 15:22:17 pm and 15:23:37 pm on Nov. 6th, 2014, with high-tide at 15:49 pm. A total of 4 measurements with speeds of $11.1, 14.8, 18.5$ and $22.2\ \mathrm{m\ s^{-1}}$ were carried out. Measurement's total time for each trial was between 65 and 117 s. It was made sure that biasing influence of other vessel operations in the surrounding was kept to a minimum. Superposition of wind waves became noticeable for the lowest speeds with small wave heights; wave breaking and splash-up at the wave gauge pole impaired the measures for the highest speed. Therefore, the recorded data of the barge, passing the gauge at the distance of 25.0 m with a speed

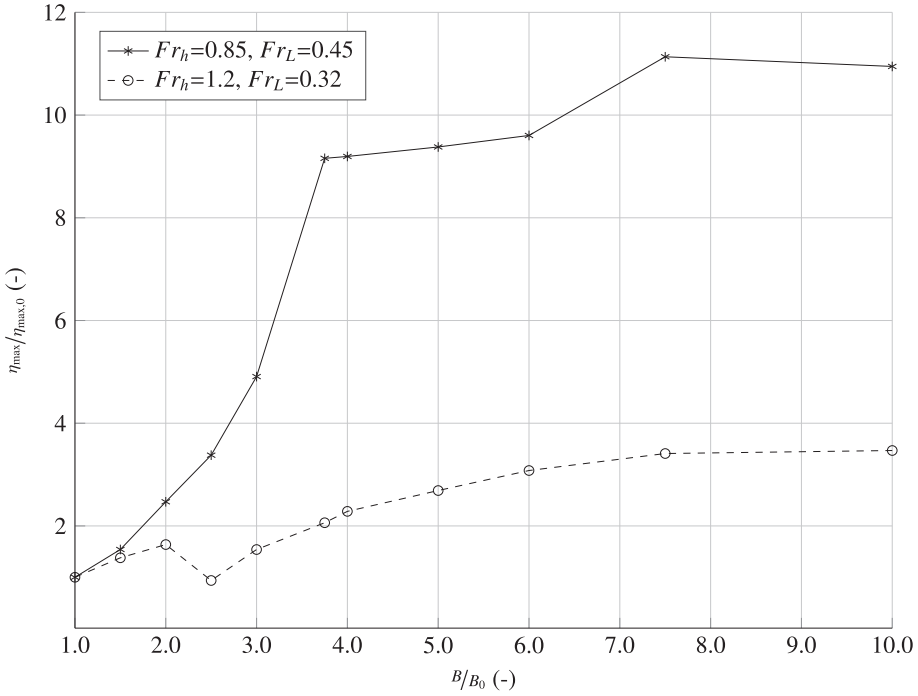

Fig. 11. Maximum water level elevation η_{max} for different pressure term widths, with an initial ship width $B_0 = 6.0$ m and a constant width $L = 60.0$ m in relation to different speeds. The data is recorded at 120 m $+0.5B$ with respect to the sailing line.

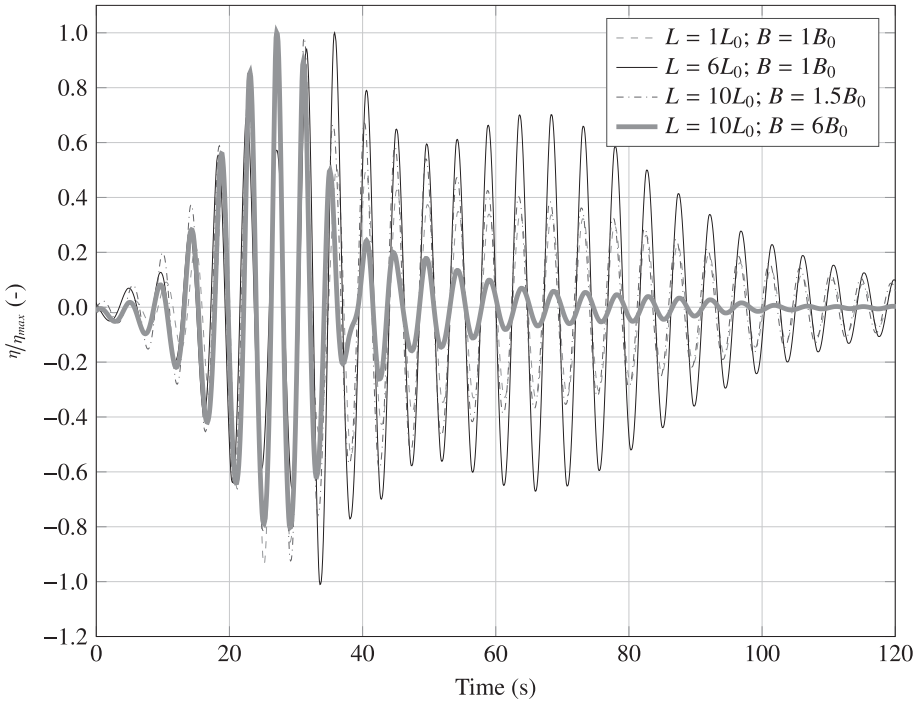

Fig. 12. Wave record for the subcritical Froude number $Fr_h = 0.85$, showing constant wave periods for different shapes of the pressure term.

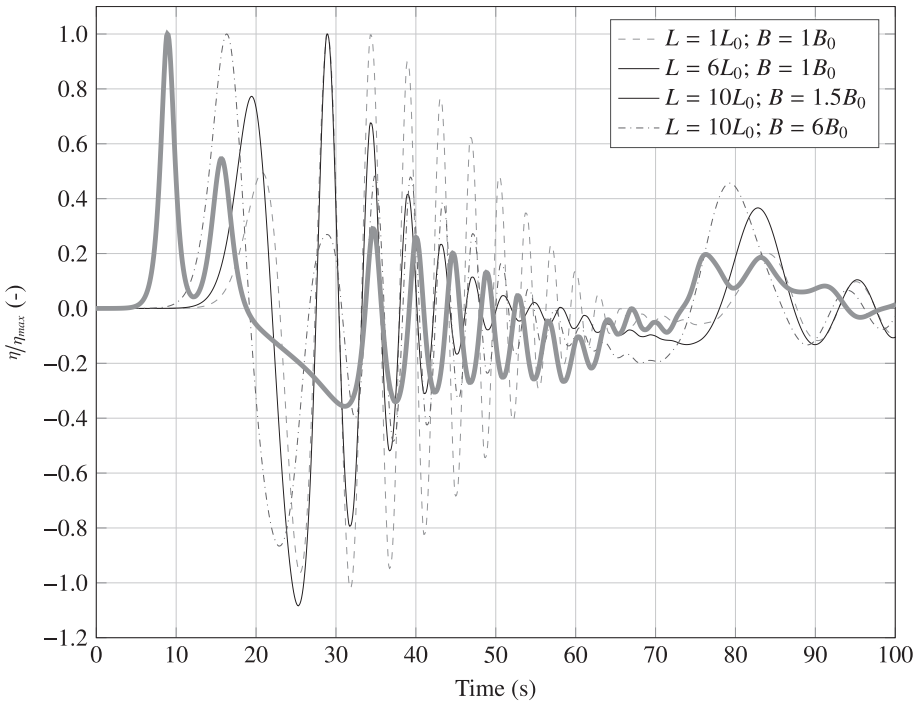

Fig. 13. Wave record for the supercritical Froude number $Fr_h = 1.20$, showing superposition of primary and secondary wave systems for pressure term ratios. A change in pressure term width has a substantial influence on wave periods of the primary wave system, but leads to only minor changes in the secondary wave system.

of 18.5 m s^{-1}, was chosen to serve as verification of the model output as bias of wind waves and non-linear dynamics at the wave gauge site was smallest. The model simulating the real-world test case close to Hamburg used a domain of 500 m × 250 m with a spatial discretization of $\Delta x = \Delta y$ =1.0 m. Fig. 15 presents photographs of the vessel used and the existing wave gauge for recording the water surface elevation; additionally a schematic of the setup used for simulation this case in BOSZ is presented along with the location of the ship's track relative to the wave gauge. The bottom of the river Elbe close to the embankment is idealized by a planar slope.

The water depth at the ship path was about $h = 8.5–9.0$ m deep, which is equivalent to $Fr_h = 0.59$. According to Equation (21), this results in $kh \approx 4.28 - 4.53$. As the waves propagate further towards the bank, water depths and thus kh will decrease. At the location of the wave gauge, the water depth was h =7.0 m at the time of the measurements, being equivalent to $kh = 3.5$. The wave conditions are well within the model's

Table 3
$\eta_{max.}$ for $\eta/\eta_{max.}$ in Figs. 12 and 13.

Run		$Fr_h = 0.85$	$Fr_h = 1.20$
		η_{max}	η_{max}
$L = L_0$;	$B = B_0$	0.1519	0.1519
$L = 6L_0$;	$B = B_0$	0.1583	0.1583
$L = 10L_0$;	$B = 1.5B_0$	0.2777	0.2933
$L = 10L_0$;	$B = 6B_0$	0.6197	1.8275

Table 4
Periods of the wave train in Fig. 13 for the sections drawdown, leading wave and the wave followed by the leading wave.

Run		T_{dd}	T_{lw}	T_{lw+1}
$L = L_0$;	$B = B_0$	4.47	5.89	4.75
$L = 6L_0$;	$B = B_0$	5.58	5.73	4.74
$L = 10L_0$;	$B = 1.5B_0$	7.51	7.04	4.67
$L = 10L_0$;	$B = 6B_0$	14.84	5.52	4.70

range of applicability.

Fig. 16 illustrates the computation result in the 2D-plane shortly after the ship has passed the wave gauge. Fig. 16 visualizes how BOSZ captures the wave processes over an irregular bathymetry, where the ship waves undergo refraction, run-up, and reflection as they interact with the sloping bank. The bathymetry was recorded by the HPA with an echo-sounder in the course of sedimentation monitoring and projected into the Universal Transverse Mercator (UTM) coordinate system, World Geodetic System standard 1984 (WGS84). The resolution is $\Delta x_{(\text{easting})} = \Delta y_{(\text{northing})} = 1$ m. The bathymetric data is a direct extraction from the raw data and is projected on the computational grid without any further smoothing or post-processing.

The wave gauge recorded the water level elevation at a sampling rate of 5 Hz while the model output was set to a rate of 10 Hz. With a wind speed of $2.7 - 3.2\ \text{ms}^{-1}$, wind-wave generated sea state was superimposed on the ship-borne waves generated by the barge's trajectory along the wave gauge. However, filtering the time-history of the surface elevation to remove wind wave components would have affected components of the ship wave signal. Therefore - apart from subtracting the mean water level from the total set for each trial - the measured water surface elevation was not post-processed any further. However, as the ratio of wind wave heights to ship waves is rather small, it was decided that the biasing effect of the wind waves present during the measurement campaign can be neglected as a first approximation.

Fig. 17 compares the above described field measurement with waves computed by BOSZ which included a pressure term representing the barge sailing by the wave gauge in the given real-world setting. Due to the grid resolution, the pressure shape was adapted to the size of the barge by setting the pressure dimensions L_s B_s and D_s to 20 m, 5 m and 1.5 m. The hull was represented with the slender ship pressure form according to Equation (17b) with the form coefficients a, λ_L and λ_B set to 16, 2, and 16 respectively.

Agreement between the modeled and the measured time-history of the surface elevation is favorable, both in terms of magnitude and phase. However, discrepancies exist between the simulated and measured surface elevation time histories in terms of a phase lag that firstly has the numerical results lag behind the in-situ measurements for the first few wave cycles; once the peak surface elevation has passed, the numerical model shows faster wave propagation as compared to the measurements. As will be furthered below, reasons for this behavior could lie within non-linear complex wave-current interaction that was not included in the model run; yet, other reasons such as inaccuracies of the available bathymetry or measurement bias (local wave breaking at the device pole) could contribute to the discrepancies. The modeled results do not include the wind waves that were present during the measurement campaign as no reliable information about the wind wave spectrum could be found to be included in the model runs. Secondly, non-linear interaction of any waves (wave breaking, transformation) in close vicinity to the pole where the wave gauge device was mounted to are not accounted for in the numerical model. A video documentation showed wave breaking at the pole after the third of the three highest waves in Fig. 17, as well occasional white capping while the ship-waves approached the device. Furthermore, the flow velocities of the river Elbe has been neglected in the computation. The ambient current was 0.53 m s^{-1}, measured by a

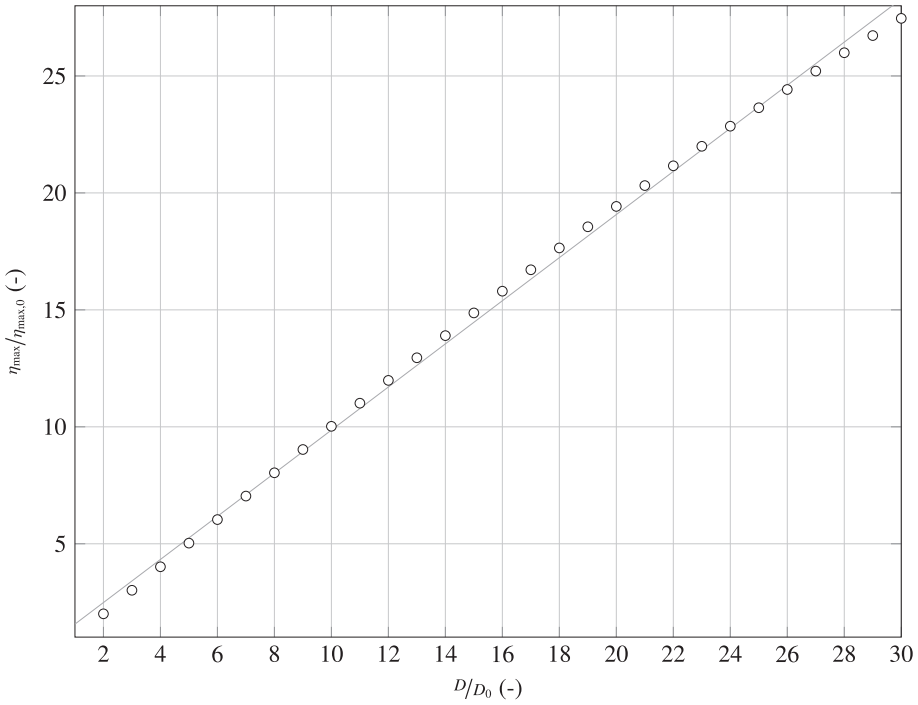

Fig. 14. Increasing the vessel's draft D, leads to an almost linear response - the line represents a linear increase - of the measured maximum free surface elevation η_{max} (circles) at position A.

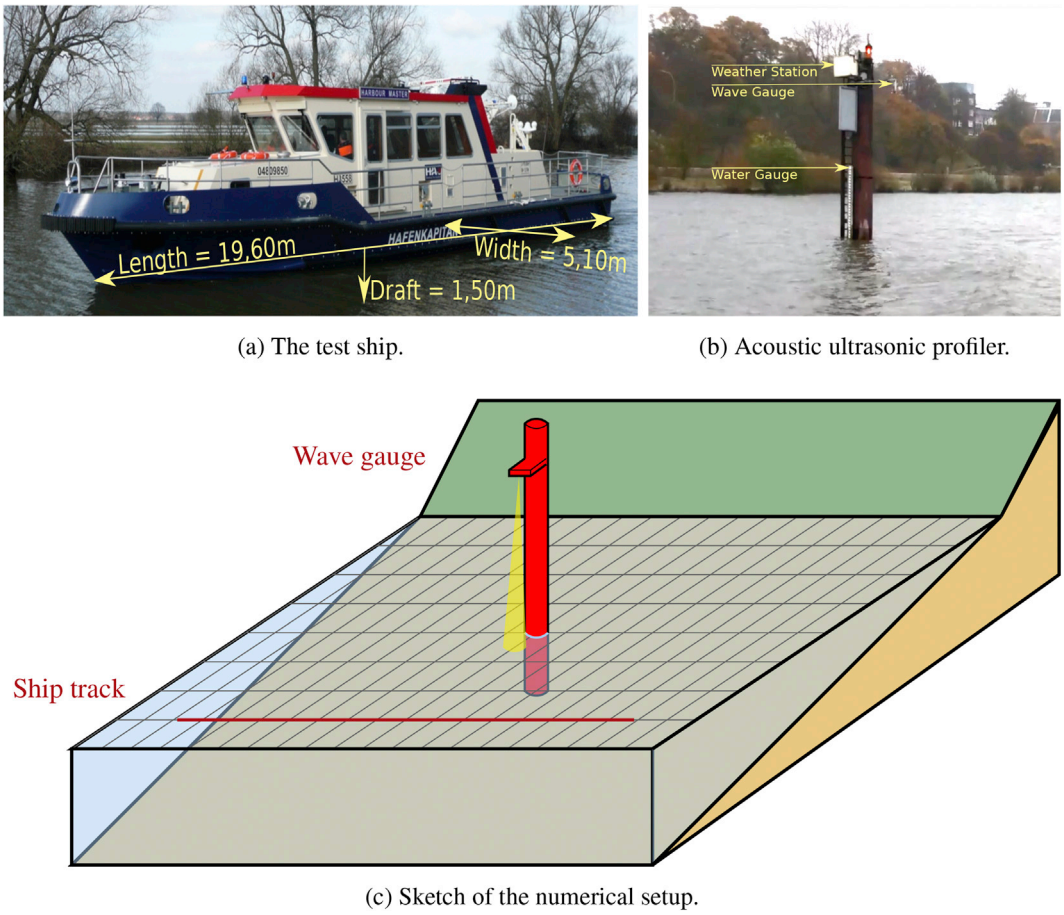

(a) The test ship. (b) Acoustic ultrasonic profiler.

(c) Sketch of the numerical setup.

Fig. 15. Ship, wave gauge, and model setup from the field campaign in the river Elbe, Hamburg. The ship passed the wave gauge along a straight path in 25 m distance to the wave gauge. An ultrasonic profiler, mounted to a steel pile, recorded the free surface elevation η at a sampling rate of 5 Hz.

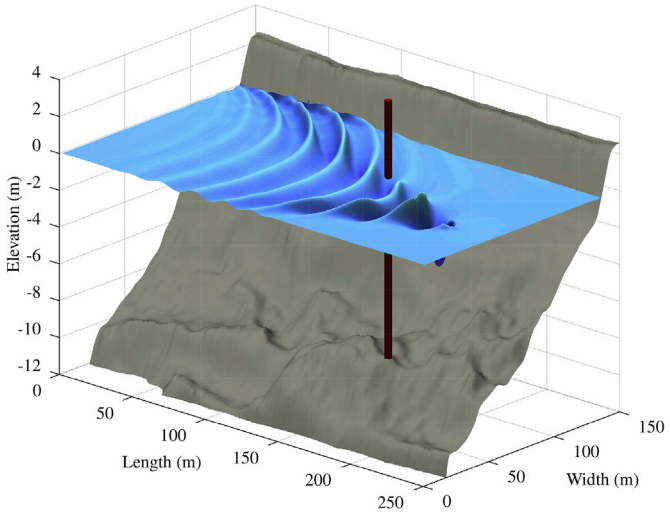

Fig. 16. Application of the model in the port of Hamburg. The figure shows the free surface elevation η, (blue) over a varying bathymetry (gray) shortly after the vessel has passed the wave gauge. The wave gauge (red) is only visualized in the figure and was not included in the computation. (For interpretation of the references to colour in this figure legend, the reader is referred to the web version of this article.)

current meter installed in Hanskalbsand, Hamburg, which is located 12.7 km downstream of the wave gauge. In addition, the measured in-situ velocity can be reduced by approximately a factor of 2 as velocities in the lateral decrease from the river thalweg towards the embankments Chow (1959). The sailing line of the vessel generating the ship wake in the test case was close to the embankment of the river (105 m away from embankment); the cross-section itself is more than 680 m wide. In comparison, no riverine discharge was added to the numerical model, potentially making up for the background currents. It is evident to include a short discussion on how the wave-current interaction is expected to influence the results: In order to quantify effects such as current-induced refraction or energy blocking a ratio of $u/\sqrt{gh}$ is commonly used (Peregrine, 1976). Peregrine (1976) stated the influence of the ambient currents on wave amplitudes for cases with uniform currents. In the present case however, a *non-uniform*, riverine background current influences the wind wave regime. Furthermore, the ship-induced wave field propagates oblique to the ambient current, not parallel as in Peregrine (1976). Furthermore, the assumed frames of reference in (Peregrine, 1976) differ to those at hand: while (Peregrine, 1976) deals with two frames of reference for motion (observer vs. wave/current), the present case comprises three different frames of reference (observer vs. wave/current vs. vessel and wave). Non-uniform, oblique attacking currents and an additional frame of reference clearly adds further complexity to the evaluation. Given the rather small ratio of ambient current to wave celerity $u/\sqrt{gh} = 0.025 - 0.04$ (using a water depth of about 9.0 m–12.0 m at the location of the instrumentation and the reduced current) in the present case, the authors argue that the ship wave field was not significantly affected and that the influence of the ambient current is fairly weak. In general, the main wave parameters of measured and modeled ship waves are in good agreement, the modeled maximum wave height $H_{max} = 0.519$ m is only 4% smaller than the measured $H_{max,gauge} = 0.541$ m. While overall agreement is favorable and reasons

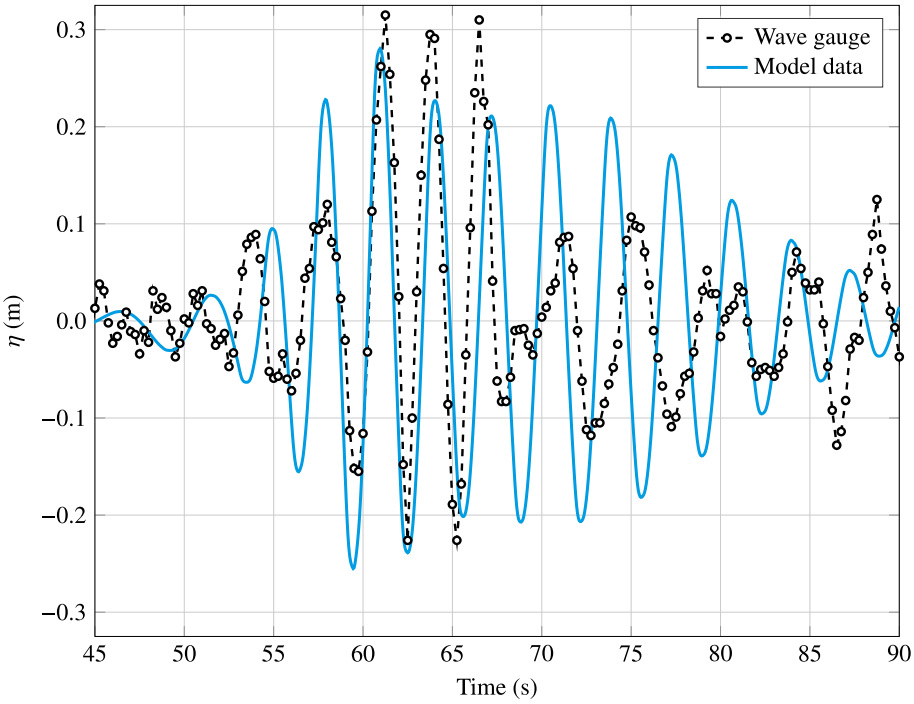

Fig. 17. Comparison of measured water level elevation η at the wave gauge. The circles denote the raw data points, connected with the dashed line, while the blue line represents the computed η. (For interpretation of the references to colour in this figure legend, the reader is referred to the web version of this article.)

for the discrepancies are discussed, it becomes evident, that further research should look into comparing results of numerical ship wave modeling; this research would most certainly benefit from additional benchmark tests originating from physical models where biasing effects as evident in the application case could be effectively prevented.

8. Summary and conclusion

This study presents the implementation of a pressure term into the governing equations of BOSZ to account for ship waves. The paper then outlines the validation of the pressure term implementation in the phase resolving, depth averaged wave model and visualizes key parameters which influence non-linear dispersive and non-dispersive ship waves. The waves generated by the pressure term technique compare well with field measures and physical experiments. Successfully validated, the model BOSZ becomes capable of modeling data from a customized field campaign in the port of Hamburg. The numerical model is thus proposed as a potential design tool, solving ship-wave related problems. Until today, coastal and hydraulic engineers have been studying moving local pressure terms (see Liu and Wu, 2004; Dam et al., 2006; Bayraktar and Beji, 2013) and have been using this approach to predict wake wave heights in confined or unconfined water bodies (see Dam et al., 2008; Soomere and Rannat, 2003; Soomere, 2007; Nascimento et al., 2011). The present study contributes to the literature by presenting convergence tests and validation scenarios and shows that ship-wake phenomena can be efficiently and accurately computed by depth-integrated models. The computations of BOSZ match the analytical solution of ship wake half angles θ_k as described in Havelock (1908). This underlines that a moving local pressure disturbance represented by an idealized ship hull is a feasible and practical methodology. This study further supports the evaluation of numerical schemes for non-linear, dispersive waves.

This paper further utilizes existing field studies and physical experiments to validate the numerical model. The implementation of pressure terms allows to determine maximum wave heights related to both Froude numbers Fr_h and Fr_L. This study provides a sensitivity analysis, which shows the model's response to changes in pressure-term dimensions. The model is able to recreate the findings of the physical experiments of Johnson (1957), who found that the wave amplitude depends on both changes of vessel dimensions and speed, while the wave shape only responds to the latter one. BOSZ confirms the design approach for waterways by BAW (2010), stating the highest water level elevation is found when vessel speed and length lead to the superposition of primary and secondary wave systems. The results also underline the findings of other studies (Sorensen, 1973; Wang and Zou, 2008; Tarafder, 2007) which correlate η_{max} to Fr_L. The maximum water level elevation η_{max} is highest, when $B > 0.375L$, while the ratio between draft and η_{max} follow a linear relation. The model is capable of reproducing multiple interacting wave train systems as well as the far-field propagation of vessel waves, shown by physical experiments and field measurements of Johnson (1957); Nece et al. (1985); Macfarlane (2012).

Ship-borne wave periods can be the driving forces for erosion and damage of waterway structures in fetch restricted waters (Houser, 2010; De Roo and Troch, 2013, 2015). Typical ship wave periods are on the order of wind waves, agreeing well with the computed wave periods in the range of $T = 5.05 - 6.62$ s (see Fig. 9) from this study. In addition, BOSZ successfully computes the waves of a vessel in the river Elbe at the entrance of the port of Hamburg. Therefore, BOSZ may serve as a suitable engineering tool for future investigations with respect to erosion and ecohydraulic problems at hand.

By both explaining the procedure of the pressure term implementation as well as by identifying the driving factors for wave heights and periods of vessel waves, this study aims at facilitating future applied research: On the one hand, the presented pressure term implementation serves as a benchmark test for phase-resolving models and can help to further validate existing codes. On the other hand, this study shows, that planners and engineers can use depth-integrated models for the design of coastal, port, and waterway assets exposed to ship-borne waves.

Acknowledgement

This study was partially funded by Hamburg Port Authority (HPA), Hamburg, Germany, and supported by the Japanese Society for the Promotion of Sciences (JSPS), Japan. C. Gabriel David was supported by the 2015 JSPS Postdoctoral Research Fellowship (Short Term), Grant

Number PE 15767. Volker Roeber is supported by JSPS KAKENHI Grant Number 15K06224 and 16K04414 (Tohoku University). Nils Goseberg acknowledges the support from a Marie Curie International Outgoing Fellowship within the 7th European Community Framework Programme (No. 622214).

We would like to specially thank Dipl.-Ing. Thomas Strothmann and Dipl.-Ing. Nino Ohle (all HPA) for organizing the field measures and supplying the data, as well as Prof. Fumihiko Imamura, Prof. Jeremy Bricker, and Midori Saito (all IRIDeS) for organizing accommodation during the JSPS program and supporting the bilateral exchange of the research team.

References

Ali, M., Murphy, K., Langendorff, J., 1999. Interrelations of river ship traffic with aquatic plants in the river nile, upper Egypt. Hydrobiologia 415, 93–100. http://dx.doi.org/10.1023/A:1003829516479. Cited By 12. https://www.scopus.com/inward/record.uri?eid=2-s2.0-0033571930&partnerID=40&md5=064ed3695be38f52526e9e5d5c9b7970.

Antuono, M., Liapidevskii, V., Brocchini, M., 2009. Dispersive nonlinear shallow-water equations. Stud. Appl. Math. 122, 1–28. http://dx.doi.org/10.1111/j.1467-9590.2008.00422.x.

Bal, S., 2008. Prediction of wave pattern and wave resistance of surface piercing bodies by a boundary element method. Int. J. Numer. Methods Fluids 56, 305–329. http://dx.doi.org/10.1002/fld.1527.

BAW, 2010. Principles for the Design of Bank and Bottom Protection for Inland Waterways (GBB). Code of Practice Federal Waterways Engineering and Research Institute of Germany Karlsruhe, Germany.

Bayraktar, D., Beji, S., 2013. Numerical simulation of waves generated by a moving pressure field. Ocean. Eng. 59, 231–239. http://dx.doi.org/10.1016/j.oceaneng.2012.12.025. http://www.sciencedirect.com/science/article/pii/S0029801812004349.

Bishop, M., 2004. A posteriori evaluation of strategies of management: the effectiveness of no-wash zones in minimizing the impacts of boat-wash on macrobenthic infauna. Environ. Manag. 34, 140–149.

Bonham, A., 1983. The management of wave-spending vegetation as bank protection against boat wash. Landsc. Plan. 10, 15–30. http://dx.doi.org/10.1016/0304-3924(83)90025-4. Cited By 18. https://www.scopus.com/inward/record.uri?eid=2-s2.0-0021055994&partnerID=40&md5=c4ebb0195afadb40c23a207540b8fdcb.

Briganti, R., Musumeci, R.E., Bellotti, G., Brocchini, M., Foti, E., 2004. Boussinesq modeling of breaking waves: description of turbulence. J. Geophys. Res. Oceans 109. http://dx.doi.org/10.1029/2003JC002065 n/a–n/a, C07015.

Brocchini, M., 2013. A reasoned overview on Boussinesq-type models: the interplay between physics, mathematics and numerics. Proc. R. Soc. A 469. http://dx.doi.org/10.1098/rspa.2013.0496.

Chen, X.-N., Sharma, S.D., 1995. A slender ship moving at a near-critical speed in a shallow channel. J. Fluid Mech. 291, 263–285. http://dx.doi.org/10.1017/S0022112095002692.

Chen, X.N., Uliczka, K., 1999. On ships in natural waterways. In: Proceedings of the RINA International Conference on Coastal Ships and Inland Waterways. London.

Chow, V.T., 1959. Open-channel Hydraulics. McGraw-Hill Book Company, New York, 680 pages.

Curtiss, G.M., Osborne, P.D., Horner-Devine, A.R., 2009. Seasonal patterns of coarse sediment transport on a mixed sand and gravel beach due to vessel wakes, wind waves, and tidal currents. Mar. Geol. 259, 73–85. http://dx.doi.org/10.1016/j.margeo.2008.12.009. http://www.sciencedirect.com/science/article/pii/S0025322709000048.

Dam, K.T., Tanimoto, K., Fatimah, E., 2008. Investigation of ship waves in a narrow channel. J. Mar. Sci. Technol. 13, 223–230. http://dx.doi.org/10.1007/s00773-008-0005-6.

Dam, K.T., Tanimoto, K., Nguyen, B.T., Akagawa, Y., 2006. Numerical study of propagation of ship waves on a sloping coast. Ocean. Eng. 33, 350–364. http://dx.doi.org/10.1016/j.oceaneng.2005.05.003.

De Roo, S., Troch, P., 2013. Field monitoring of ship wave action on environmentally friendly bank protection in a confined waterway. J. Waterw. Port. Coast. Ocean. Eng. 139, 527–534. http://dx.doi.org/10.1061/(ASCE)WW.1943-5460.0000202.

De Roo, S., Troch, P., 2015. Evaluation of the effectiveness of a living shoreline in a confined, non-tidal waterway subject to heavy shipping traffic. River Res. Appl. 31, 1028–1039. http://dx.doi.org/10.1002/rra.2790.

Fang, M.-C., Yang, R.-Y., Shugan, I.V., 2011. Kelvin ship wake in the wind waves field and on the finite sea depth. J. Mech. 27, 71–77. http://dx.doi.org/10.1017/jmech.2011.9. http://journals.cambridge.org/article_S1727719111000098.

Franzius, O., Straub, L., 1936. Waterway Engineering: a Text and Handbook Treating of the Design, Construction, and Maintenance of Navigable Waterways. Technology Press, Massachusetts Institute of Technology.

Gates, E., Herbich, J., 1977. Mathematical Model to Predict the Behavior of Deep-draft Vessels in Restricted Waterways. Report TAMU-SG-77-206. Texas A&M University.

Gottlieb, S., Shu, C.-W., Tadmor, E., 2001. Strong stability-preserving high-order time discretization methods. SIAM Rev. 43, 89–112. http://dx.doi.org/10.1137/S003614450036757X.

Havelock, T.H., 1908. The propagation of groups of waves in dispersive media, with application to waves on water produced by a travelling disturbance. In: Proceedings of the Royal Society A, vol. 81. The Royal Society, pp. 398–430. http://dx.doi.org/10.1098/rspa.1908.0097.

Houser, C., 2010. Relative importance of vessel-generated and wind waves to salt marsh erosion in a restricted fetch environment. J. Coast. Res. 230–240. http://dx.doi.org/10.2112/08-1084.1.

Johnson, J., 1957. Ship waves in navigation channels. In: Coastal Engineering Proceedings, vol. 6, p. 40. https://icce-ojs-tamu.tdl.org/icce/index.php/icce/article/view/2034.

Kim, S., Lee, S., Kim, K.H., 2008. Wavenumber-extended high-order oscillation control finite volume schemes for multi-dimensional aeroacoustic computations. J. Comput. Phys. 227, 4089–4122. http://dx.doi.org/10.1016/j.jcp.2007.12.013. http://www.sciencedirect.com/science/article/pii/S0021999107005657.

Li, Y., Sclavounos, P.D., 2002. Three-dimensional nonlinear solitary waves in shallow water generated by an advancing disturbance. J. Fluid Mech. 470, 383–410. http://dx.doi.org/10.1017/S0022112002001568. http://journals.cambridge.org/article_S0022112002001568.

Liu, P.L.-F., Wu, T.-R., 2004. Waves generated by moving pressure disturbances in rectangular and trapezoidal channels. J. Hydraulic Res. 42, 163–171. http://dx.doi.org/10.1080/00221686.2004.9728379. http://www.tandfonline.com/doi/abs/10.1080/00221686.2004.9728379.

Lord Kelvin (William Thomson), 1887. On ship waves. In: Proceedings of the Royal Society of Edinburgh, vol. 38, pp. 409–434.

Lynett, P., Liu, P.L., 2004. A two-layer approach to wave modelling. Proc. R. Soc. A 460, 2637–2669. http://dx.doi.org/10.1098/rspa.2004.1305.

Macfarlane, G.J., 2012. Marine Vessel Wave Wake: Focus on Vessel Operations within Sheltered Waterways. Technical Report. Australian Maritime College, University of Tasmania.

Madsen, P.A., Murray, R., Sörensen, O.R., 1991. A new form of the boussinesq equations with improved linear dispersion characteristics. Coast. Eng. 15, 371–388. http://dx.doi.org/10.1016/0378-3839(91)90017-B. http://www.sciencedirect.com/science/article/pii/037838399190017B.

Madsen, P.A., Soerensen, O.R., 1992. A new form of the boussinesq equations with improved linear dispersion characteristics. part 2. a slowly-varying bathymetry. Coast. Eng. 18, 183–204. http://dx.doi.org/10.1016/0378-3839(92)90019-Q. http://www.sciencedirect.com/science/article/pii/037838399290019Q.

Miyata, H., Nishimura, S., 1985. Finite-difference simulation of nonlinear ship waves. J. Fluid Mech. 157, 327–357.

Nakos, D., Sclavounos, P., 1994. Kelvin wakes and wave resistance of cruiser- and transom-stern ships. J. Ship Res. 38, 9–29.

Nascimento, M.F., Neves, C., Maciel, G., 2011. Waves generated by two or more ships in a channel. Coast. Eng. Proc. 1, 60. https://journals.tdl.org/icce/index.php/icce/article/view/1441.

Nascimento, M.F., Neves, C.F., de Freitas Maciel, G., 2009. Propagation of ship waves on a sloping bottom. In: Conference: Coastal Engineering 2008. http://dx.doi.org/10.1142/9789814277426_0059.

Nece, R.E., McCaslin, M.R., Christensen, D., 1985. Ferry Wake Study. Final Report WA-RD-70.1 Washington State Transportation Center Washington State Transportation Center. Department of Civil Engineering, University of Washington, Seattle, Washington.

Nwogu, O., 1993. Alternative form of boussinesq equations for nearshore wave propagation. J. Waterw. Port, Coast. Ocean Eng. 119, 618–638. http://dx.doi.org/10.1061/(ASCE)0733-950X(1993)119:6(618).

Ohle, N., Zimmermann, C., 2001. Restoration of a tidal river embankment. In: Phelps, D., Shelke, G. (Eds.), Bridging the Gap: Meeting the World's Water and Environmental Resources Challenges World Water and Environmental Resources Congress. American Society of Civil Engineers, The Rosen Plaza Hotel, Orlando, Florida, United States.

Peregrine, D.H., 1967. Long waves on a beach. J. Fluid Mech. 27, 815–827. http://dx.doi.org/10.1017/S0022112067002605. http://journals.cambridge.org/article_S0022112067002605.

Peregrine, D.H., 1976. Interaction of water waves and currents. Adv. Appl. Mech. 16, 9–117.

PIANC, 1987. Guide- Lines for the Design and Construction of Flexible Revetments Incorporating Geotextiles for Inland Waterways. Technical Report. Permanent International Association of Navigation Congresses.

Ravens, T., Thomas, R., 2008. Ship wave-induced sedimentation of a tidal creek in galveston bay. J. Waterw. Port, Coast. Ocean Eng. 134, 21–29. http://dx.doi.org/10.1061/(ASCE)0733-950X(2008)134:1(21).

Roeber, V., Bricker, J.D., 2015. Destructive tsunami-like wave generated by surf beat over a coral reef during typhoon haiyan. Nat. Commun. 6 http://dx.doi.org/10.1038/ncomms8854.

Roeber, V., Cheung, K.F., 2012. Boussinesq-type model for energetic breaking waves in fringing reef environments. Coast. Eng. 70, 1–20. http://dx.doi.org/10.1016/j.coastaleng.2012.06.001. http://www.sciencedirect.com/science/article/pii/S0378383912001081.

Roeber, V., Cheung, K.F., Kobayashi, M.H., 2010. Shock-capturing boussinesq-type model for nearshore wave processes. Coast. Eng. 57, 407–423. http://dx.doi.org/10.1016/j.coastaleng.2009.11.007. http://www.sciencedirect.com/science/article/pii/S0378383909001860.

Schiereck, G., 2001. Introduction to Bed, Bank and Shore Protection. Delft University Press, Delft, The Netherlands. ISBN 90-407-1683-8.

Shi, F., Kirby, J.T., Harris, J.C., Geiman, J.D., Grilli, S.T., 2012. A high-order adaptive time-stepping tvd solver for boussinesq modeling of breaking waves and coastal inundation. Ocean. Model. 43 – 44, 36–51. http://dx.doi.org/10.1016/j.ocemod.2011.12.004. http://www.sciencedirect.com/science/article/pii/S1463500311002010.

Silinski, A., Heuner, M., Schoelynck, J., Puijalon, S., Schröder, U., Fuchs, E., Troch, P., Bouma, T., Meire, P., Temmerman, S., 2015. Effects of wind waves versus ship waves on tidal marsh plants: a flume study on different life stages of scirpus maritimus. PLoS One 10. http://dx.doi.org/10.1371/journal.pone.0118687.

Simarro, G., Orfila, A., Galan, A., 2013. Linear shoaling in Boussinesq-type wave propagation models. Coast. Eng. 80, 100–106.

Soomere, T., 2007. Nonlinear components of ship wake waves. Appl. Mech. Rev. 60, 120–138. http://dx.doi.org/10.1115/1.2730847.

Soomere, T., Rannat, K., 2003. An experimental study of wind waves and ship wakes in Tallinn Bay. In: Proceedings of the Estonian Academy of Sciences, Engineering, vol. 9, p. 157. http://search.ebscohost.com/login.aspx?direct=true&db=aph&AN=10953844&lang=ja&site=ehost-live.

Sorensen, R.M., 1973. Ship-generated waves. In: Chow, V.T. (Ed.), Advances in Hydroscience, vol. 9. Academic Press Inc, pp. 49–83.

Sorensen, R.M., 1997. Prediction of vessel-generated waves with reference to vessels common to the upper Mississippi river system. ENV Report 4. Department of Civil and Environmental Engineering Lehigh University, Bethlehem, PA, p. 18015.

Tarafder, S., 2007. Third order contribution to the wave-making resistance of a ship at finite depth of water. Ocean. Eng. 34, 32–44. http://dx.doi.org/10.1016/j.oceaneng.2006.01.007. http://www.sciencedirect.com/science/article/pii/S0029801806000801.

Toro, E.F., 2009. Riemann Solvers and Numerical Methods for Fluid Dynamics: a Practical Introduction, third ed. Springer, Berlin, New York. http://dx.doi.org/10.1017/jmech.2011.9.

Torsvik, T., Didenkulova, I., Soomere, T., Parnell, K.E., 2009. Variability in spatial patterns of long nonlinear waves from fast ferries in Tallinn Bay. Nonlinear Process. Geophys. 16, 351–363. http://dx.doi.org/10.5194/npg-16-351-2009. In: http://www.nonlin-processes-geophys.net/16/351/2009/.

Velegrakis, A., Vousdoukas, M., Vagenas, A., Karambas, T., Dimou, K., Zarkadas, T., 2007. Field observations of waves generated by passing ships: a note. Coast. Eng. 54, 369–375. http://dx.doi.org/10.1016/j.coastaleng.2006.11.001.

Verhagen, H.J., 1998. Dikes and revetments: design, maintenance and safety assessment. In: Chapter Hydraulic Boundary Conditions. A.A. Balkema, pp. 41–74.

Verhey, H., Bogaerts, M., 1989. Ship waves and the stability of armour layers protecting slopes. In: Proceedings of the 9th International Harbor Congress. Antwerp, Belgium.

Wang, H., Zou, Z.-j., 2008. Numerical research on wave-making resistance of trimaran. J. Shanghai Jiaot. Univ. Sci. 13, 348–351. http://dx.doi.org/10.1007/s12204-008-0348-5.

Weggel, J., Sorensen, R.M., 1986. Ship wave prediction for port and channel design. In: Sorensen, P.H. (Ed.), Proceedings of the Ports '86 Conference. American Society of Civil Engineers, Oakland, CA, pp. 797–814.

Wei, G., Kirby, J.T., 1995. Time-dependent numerical code for extended boussinesq equations. J. Waterw. Port, Coast. Ocean Eng. 121 http://dx.doi.org/10.1061/(ASCE)0733-950X(1995)121:5(251).

Witting, J.M., 1984. A unified model for the evolution nonlinear water waves. J. Comput. Phys. 56, 203–236. http://dx.doi.org/10.1016/0021-9991(84)90092-5. http://www.sciencedirect.com/science/article/pii/0021999184900925.

Zhu, Y., He, J., Zhang, C., Wu, H., Wan, D., Zhu, R., Noblesse, F., 2015. Farfield waves created by a monohull ship in shallow water. Eur. J. Mech. - B/Fluids 49 (Part A), 226–234. http://dx.doi.org/10.1016/j.euromechflu.2014.09.006. http://www.sciencedirect.com/science/article/pii/S0997754614001460.